ACTUATORS

A buckling-sheet ring oscillator for electronics-free, multimodal locomotion

Won-Kyu Lee[1]†, Daniel J. Preston[1,2]†, Markus P. Nemitz[1,2], Amit Nagarkar[1], Arthur K. MacKeith[1], Benjamin Gorissen[3], Nikolaos Vasios[3], Vanessa Sanchez[2,3], Katia Bertoldi[3], L. Mahadevan[3,4,5], George M. Whitesides[1,2,5]*

Locomotion of soft robots typically relies on control of multiple inflatable actuators by electronic computers and hard valves. Soft pneumatic oscillators can reduce the demand on controllers by generating complex movements required for locomotion from a single, constant input pressure, but either have been constrained to low rates of flow of air or have required complex fabrication processes. Here, we describe a pneumatic oscillator fabricated from flexible, but inextensible, sheets that provides high rates of airflow for practical locomotion by combining three instabilities: out-of-plane buckling of the sheets, kinking of tubing attached to the sheets, and a system-level instability resulting from connection of an odd number of pneumatic inverters made from these sheets in a loop. This device, which we call a "buckling-sheet ring oscillator" (BRO), directly generates movement from its own interaction with its surroundings and consists only of readily available materials assembled in a simple process—specifically, stacking acetate sheets, nylon film, and double-sided tape, and attaching an elastomeric tube. A device incorporating a BRO is capable of both translational and rotational motion over varied terrain (even without a tether) and can climb upward against gravity and downward against the buoyant force encountered under water.

INTRODUCTION

Almost all locomotion in soft robotic systems functioning at useful scales relies on pneumatic or hydraulic actuators (*1–7*). The locomotion of soft robots using these fluidic actuators requires periodic pressurization and depressurization (i.e., oscillation) of multiple pressure sources (*1, 3, 8*), which is currently achieved primarily using hard solenoid valves controlled by electronic devices and circuits (*6, 8, 9*). Although achieving a reduced number of control elements is possible by leveraging fluidic resistance in soft robots (*10, 11*), advanced biomimetic locomotion—including climbing upward against gravity, downward, underwater, or against buoyant force—has still relied on multiple tethered inputs from pressure sources regulated and synchronized by complex control systems (*9, 12–16*). Hydraulically amplified electrostatic actuators and artificial muscles have enabled locomotion of soft robots over varied terrain; however, these systems require relatively high operating voltages that need to be carefully insulated in underwater environments (*17–19*).

To realize autonomous locomotion of soft robots without the need for electronic controls and hard valves (i.e., locomotors with a low level of autonomy), soft pneumatic and hydraulic oscillators have been created using microfluidic platforms (*20–22*) and elastomeric valves (*2, 3*); these oscillators convert a constant input pressure to a time-varying output pressure and have been integrated in fully soft devices to generate motion (*3, 22*). Microfluidic control devices, however, are not suitable for mesoscale (i.e., length scales larger than a few centimeters) pneumatic robots and machines because low rates of airflow, due to drag in channels with small internal sizes, limit actuation speed (*3, 22*). Perhaps more importantly, microfluidic devices are fabricated via lithographic approaches (e.g., soft lithography) (*23–25*); integration with mesoscale fabrication tools [e.g., three-dimensional (3D) printing or layer-based assembly] complicates fabrication processes (*23–25*). For example, during fabrication of "octobot," the microfluidic oscillator was fabricated separately and then integrated with the 3D-printed main body manually (*22*).

We have developed a soft, bistable valve for autonomous control of soft actuators (*3*), and we used this valve to form reconfigurable digital logic gates and circuits that enable relatively simple human-robot interaction and environmental sensing in soft robots (*2*). Furthermore, we demonstrated an elastomeric ring oscillator using an odd number of these valves—configured as inverters—connected in a loop (*1*), which enabled coordinated periodic motion of several external soft actuators using a single, constant-pressure input. This elastomeric ring oscillator must be connected to separate soft actuators to achieve locomotion (*1–3*) (this requirement does, however, increase system complexity in the design of soft robots). In addition, the fabrication of the elastomeric valves comprising the oscillator requires a multistep molding and manual assembly procedure (*1–3*)—complexities that may limit ease of fabrication and large-scale integration. With these limitations in mind, development of the simplest actuation system (in terms of structure and fabrication processes) to control pressures and flows of air large enough to operate mesoscale soft robots is important.

We recently demonstrated that leveraging a reversible buckling instability can allow thin circular sheets to crawl on land and swim on water upon application of oscillatory pressures generated by solenoid valves controlled by an electronic computer (*26*). Although

[1]Department of Chemistry and Chemical Biology, Harvard University, 12 Oxford Street, Cambridge, MA 02138, USA. [2]Wyss Institute for Biologically Inspired Engineering, 3 Blackfan Circle, Boston, MA 02115, USA. [3]School of Engineering and Applied Sciences, Harvard University, 29 Oxford Street, Cambridge, MA 02138, USA. [4]Department of Physics, Department of Organismic and Evolutionary Biology, Harvard University, 17 Oxford Street, Cambridge, MA 02138, USA. [5]Kavli Institute for Bionano Science and Technology, Harvard University, 29 Oxford Street, Cambridge, MA 02138, USA.
*Corresponding author. Email: gwhitesides@gmwgroup.harvard.edu
†These authors contributed equally to this work.

complex electro-pneumatic control devices are still necessary to control these simple buckling sheets, both the structure of the sheets and the fabrication processes are simple—the locomotor consists only of readily available materials assembled in a one-step process (i.e., stacking of acetate sheets, nylon film, and double-sided tape). In particular, although we only demonstrated the capability of these sheets as locomotors, they could also serve as a platform to create mechanofluidic transistors, in essence functioning as slender pneumatic valves. Pneumatic circuits, including multiple buckling sheets configured as logic elements, could ultimately realize electronics-free locomotion, thereby addressing the complexity and other issues observed in the previous bistable valves and associated pneumatic control approach.

In this work, we created a buckling-sheet ring oscillator (BRO) that converts a constant input pressure to temporally offset coordinated oscillation of the internal pressures of multiple buckling sheets, and thereby either induces locomotion directly from the undulating motions of the BRO itself as it interacts with its surroundings or controls actuators with its oscillating internal pressures to enable locomotion. The BRO is composed of buckling-sheet inverters (as single-level devices), each of which consists only of four simple components, including an acetate sheet (i.e., a cellulose acetate overhead transparency film), a thin nylon film, elastomeric tubing, and double-sided tape. We fabricated buckling-sheet inverters by assembling—via stacking and pressing—these commercially available materials. We then formed the BRO by connecting an odd number of the inverters to each other in a loop. Our robotic ring oscillator can move over plastic, cloth, and sand, and at an air-water interface, without any added actuators, via translational and rotational locomotion induced directly by the buckling of its component sheets. By supplementing the BRO with additional buckling-sheet actuators (BSAs) to amplify its ability to generate motion, we demonstrated motion up an incline against gravity using only a single, constant pressure input, which has been difficult for previously reported robotic systems to achieve (*9*, *12*, *15*). As a prototypic, practical use of the BRO, we show that it can descend into water against buoyancy to perform cleaning of underwater supports. Other applications may extend to collection of biological specimens, pipeline inspection, and management of undersea assets (*27*, *28*).

RESULTS

Buckling sheet as a pneumatic inverter

We used a flexible plastic sheet with an attached pneumatic bladder as a platform to develop a pneumatic buckling-sheet inverter (Fig. 1). The buckling-sheet inverter takes advantage of the reversible buckling of thin sheets, which are flexible but not extensible. These buckling sheets remain in a flat, 2D configuration when unactuated, but generate out-of-plane topography when actuated (*29*, *30*). They operate on the principle that stretching a sheet requires much more energy than bending it (*29*, *30*); for example, pushing the center of a circular transparency sheet into a circular opening, for instance, the top of a drinking cup, generates 3D buckles along the radial direction (*29*, *30*).

The buckling sheets used here each consist of a circular sheet of poly(cellulose acetate) and a circular pneumatic bladder, attached with double-sided tape (Fig. 1) in a process similar to that used in prior work to create a simple buckling sheet (*26*). Thin rubber tubing connects the bladder to an external pneumatic source. When the bladder is pressurized, it expands in volume, stressing the entire transparent sheet. The sheet responds by bending out of plane and breaking its radial symmetry to form a puckered geometry that is polarized and has reflection symmetry (*29*). The polarization of the buckling instability that appears in the sheet is random on an ideal, pristine sheet; however, we can manually control the desired polarization of the buckling instability by locally folding—and (slightly) plastically deforming—the transparency sheet. After this initial "programming," the sheet always buckles reversibly into the same shape, making it a reliable and mechanically programmable actuator.

To develop a pneumatic inverter from the buckling sheet, we attached a pneumatic flow-control tube on the surface of the sheet to guide the buckling (the blue tubing in Fig. 1A and fig. S1). The flow-control tube kinks when an input pressure (P_{IN}) to the bladder of the buckling sheet (which behaves as a pneumatic capacitor) is greater than the threshold of 10 kPa required for complete buckling (P_{BUCK}) of the sheet ($P_{IN} > P_{BUCK} = 10$ kPa, where 100 kPa = 1 atm). In this buckled state ($P_{IN} > P_{BUCK}$), the output pressure (P_{OUT}) from the kinked flow-control tube attached to the sheet is equal to zero ("off" state), regardless of the supply pressure at the inlet of the flow-control tube (P_{SUPP}). The output pressure (P_{OUT}) from the flow-control tube becomes equal to P_{SUPP} when the input pressure to the bladder of the buckling sheet is lower than the threshold for complete unfolding of 6 kPa ($P_{IN} < P_{UNFOLD} = 6$ kPa), where the buckling-sheet inverter unfolds ("on" state). This switching mechanism of the buckling-sheet inverter is analogous to that achieved by an electronic transistor, where the absence or presence of an input pressure (analogous to gate voltage) opens or closes a pathway for airflow (analogous to current) (*31*).

The importance of a "resistor" in the buckling-sheet inverter is also analogous to an electronic device: An electronic inverter is composed of both a transistor and a resistor. The electronic resistor, which connects the output of the electronic inverter to ground, prohibits an indeterminate "floating" output state when the electronic inverter input takes a value of zero; this resistor is often referred to as a "pulldown resistor" (*32*). The pneumatic version shown here uses the pneumatic transistor, described above, combined with a length of tubing with a thin (0.8 mm) inner diameter to provide resistance to airflow (Fig. 1B). The pneumatic pulldown resistor connecting P_{OUT} from the buckling-sheet inverter to pneumatic ground (atmospheric pressure, P_{ATM}) is critical; without it, the output state would always remain at the supply pressure, P_{SUPP}, after the first actuation.

Hysteretic switching behavior of the buckling-sheet inverter

We characterized the switching of the buckling-sheet inverter by measuring P_{OUT} as a function of a continuously varying input pressure P_{IN} (Fig. 1B). We found that the output P_{OUT} decreases to a low value when $P_{IN} > P_{BUCK}$, and the output P_{OUT} increases to a high value when $P_{IN} < P_{UNFOLD}$, independent of the constant (but different) values of P_{BUCK} and P_{UNFOLD}, and regardless of P_{SUPP} (fig. S2). This switching behavior with hysteresis is similar to that of the bistable valve shown in our prior work (*1–3*), where hysteresis from the bistable valve allows oscillation. Compared with the "binary" switching of the bistable valve, however, the sigmoid pattern of hysteresis from the buckling-sheet inverter exhibits "continuous" switching between the threshold values of P_{UNFOLD} and P_{BUCK}. Specifically, P_{OUT} will take every value between its high and low
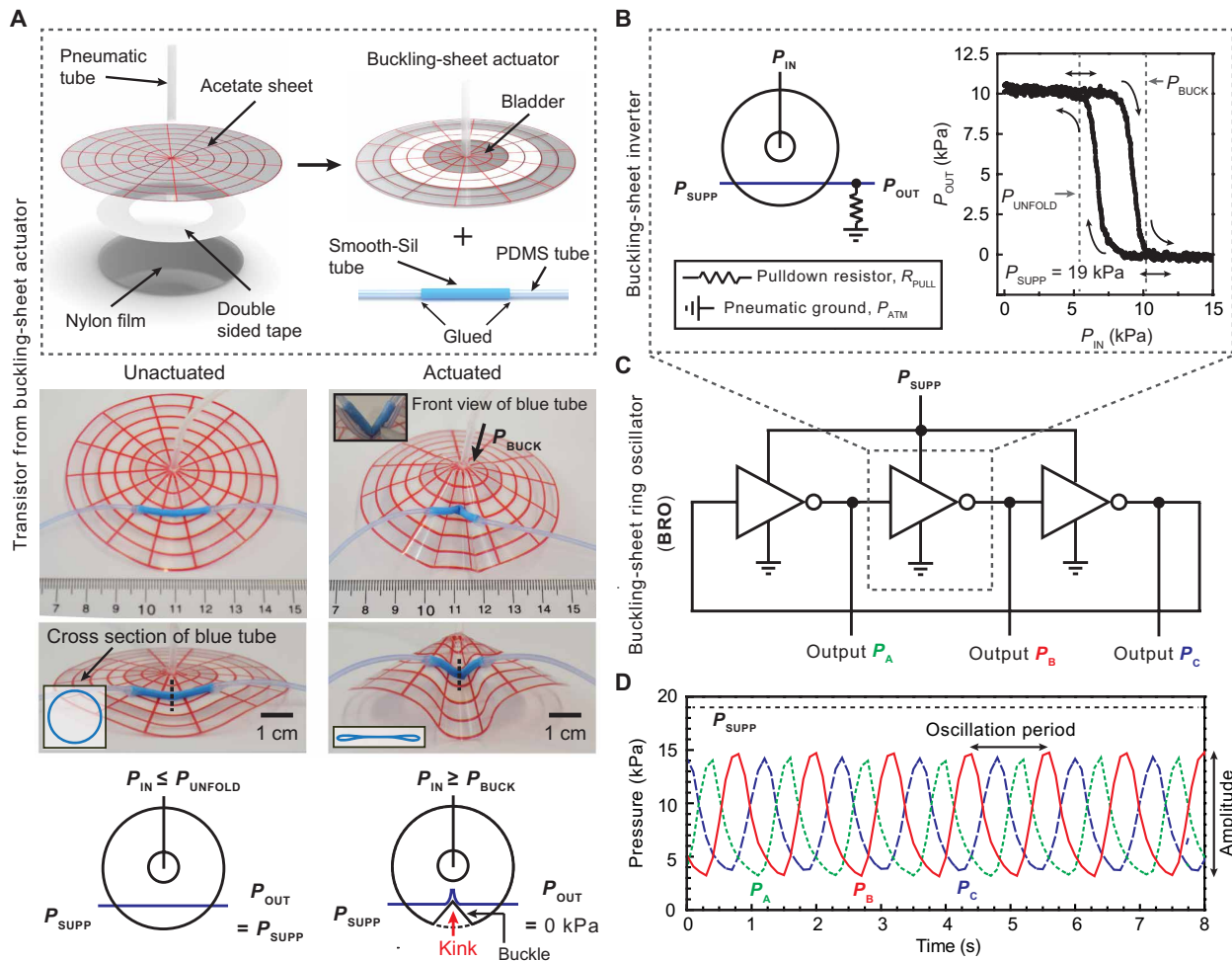
Fig. 1. Pneumatic inverter and ring oscillator from BSA. Fabrication processes for BSAs (top schematics) and photos of a buckling-sheet inverter before and after actuation (middle) with corresponding schematics (bottom) and with the flow-control (blue) tubing attached (**A**). The system works as a pneumatic inverter by connecting a pulldown resistor (**B**); the system was characterized by recording output pressure (P_{OUT}) as a function of varying input pressure (P_{IN}) under a constant supply pressure (P_{SUPP}) of 19 kPa. Three buckling-sheet inverters were connected to each other in a loop to form a ring oscillator (**C**). The ring oscillator generated temporally coordinated undulating output pressures P_A (green), P_B (red), and P_C (blue) when a single, constant input pressure, P_{SUPP}, was applied (**D**).

states as the input pressure, P_{IN}, is increased from its low to high state. In this regime, the buckling-sheet inverter mirrors an inverting amplifier in an electronic circuit (*32*). Operation with the input constrained to either the high or low state (as in binary digital logic) reduces the operation of the buckling sheet to that of a simple inverter.

The hysteretic switching of the buckling-sheet inverter originates from the geometric hysteresis inherent in the viscoelastic substrate (i.e., the transparency sheet) during buckling and unfolding (fig. S3). We measured the bending angle (θ) of the flow-control tube at the center of the buckling position. During the buckling process, θ decreased almost linearly with input pressure, P_{IN}, from θ = 145° to θ = 75° as P_{IN} increased from 0 to 10.5 kPa (just over the pressure required to kink the attached tubing, P_{BUCK} = 10 kPa), at which point the flow-control tube completely kinks and prevents the flow of air. We observed a further decrease in θ as P_{IN} increased beyond P_{BUCK}, even after airflow through the tubing was completely blocked at θ = 75°, down to a minimum value of θ = 60° under an applied input pressure, P_{IN}, of 14 kPa (fig. S3). As the buckling-sheet

inverter unfolds, θ increases from its minimum value to a value of 90° when P_{IN} = P_{UNFOLD}. The θ values during unfolding are always smaller than those during buckling with the same P_{IN} as a consequence of hysteresis (fig. S3). Using a finite element method model of our system, we further calculated cross-sectional areas of the kinking region of the flow-control tube during inverter pressurization and depressurization (fig. S4 and movies S1 and S2). The hysteresis in these cross-sectional areas as a function of P_{IN} was similar to that of the θ values. We attributed the hysteresis to the combined effect of the subcritical bifurcation associated with the kinking of the tubing and the damping of the viscoelastic substrate materials, i.e., the poly(cellulose acetate) sheet and the tubing.

We also characterized the buckling-sheet inverter by applying a varying input pressure, P_{IN}, with a time interval of 5-s on, 5-s off (with constant P_{SUPP}), during which time we measured P_{OUT} (fig. S5). Despite the delay in signal switching associated with the inflation of the bladder in the buckling-sheet inverter (resulting from pneumatic capacitance) and the resistance to airflow within the tubing, the output pressure P_{OUT} varied with an almost identical time interval

of 5 s. This regularity confirms the reliability of pneumatic mechanical switching based on buckling. P_{OUT} was slightly lower than P_{SUPP} because of the pressure drop associated with the pulldown resistor. The output pressure P_{OUT} must necessarily be lower than the supply pressure P_{SUPP} because of the pressure drop associated with the pulldown resistor, following the same physical principle as the electrical circuit analog. However, as long as P_{OUT} is greater than the pressure (P_{BUCK}) required to buckle the sheet, an unlimited number of buckling-sheet inverters may be connected in series. The output from a single buckling-sheet inverter may also be used to control an unlimited number of other buckling-sheet inverters, actuators, or other components; the response time in this case, however, would accordingly be slowed as the pneumatic capacitance increases when controlling more devices.

Compared with previously reported bistable valves (3), our transistor-type buckling-sheet inverter offers the advantage of continuous control of pressure, resulting in smoother motion of pneumatic soft robots. The switching behavior of the buckling-sheet inverter does not exhibit snap-through behavior between the two states, in contrast to the bistable valve, where a snap-through instability is used to generate quick motions of a bistable membrane inside the valve and gives rise to two discrete states (e.g., "0" and "1") (1–3); rather, P_{OUT} transitions continuously from a high to low state as a function of increasing P_{IN}, which is similar to transistor-transistor logic gates. The advantage of this monotonic and continuous switching from the transistor-type buckling-sheet inverter is that we can access intermediate states between 0 and 1 not possible by truly "digital" control from the bistable valve, although we must apply a constant flow of pressurized air to the input of the bladder to maintain the pneumatic state as a consequence of the required pulldown resistor, thus decreasing the energy efficiency of the system. Because the locomotion of the buckling sheet (corresponding to repeated buckling and unfolding) arises from pressurization over only half of the cycle (i.e., buckling of the sheet) while allowing the system to recover passively over the other half of the cycle (i.e., unfolding of the sheet), the conversion of energy from pressurized air to locomotion is relatively efficient (26). Furthermore, the pressurized air exhausted from the bladders of the buckling-sheet inverters during repeated cycling can be repurposed for use in a multifunctional robotic system (as shown below in an aquatic environment), highlighting an important advantage of the mechanofluidic transistor framework compared with electronic approaches.

A BRO from multiple buckling-sheet inverters
We designed the BRO with three buckling-sheet inverters connected in a loop (Fig. 1C). Here, the output P_{OUT} of one inverter acts as the input P_{IN} of the next inverter such that the inverters take alternating buckled and unfolded states. To create the "ring," the output from the last inverter in the series is connected to the input of the first inverter (fig. S6). When the supply pressure, P_{SUPP}, was first applied, an initial transient state lasting 2 s was observed during which all three inverters started to buckle before the generation of the instability. No stable state exists for this type of system (whether electronic, pneumatic, or mechanical), and a pneumatic instability travels along the ring as inverters sequentially buckle and unfold. The ring oscillator always contains either two adjacent unfolded inverters (with one inverter in the process of buckling) or two adjacent buckled inverters (with one inverter in the process of unfolding) (fig. S6). During the alternation between these two dynamic states

in the system, the instability travels along the ring. This propagating instability leads to periodic, temporally coordinated oscillation of the outputs [i.e., the output pressures for a three-inverter ring oscillator are $P_A(t)$, $P_B(t + \delta)$, and $P_C(t + 2\delta)$, where δ is one-third the period of oscillation].

When we applied a supply of compressed air at constant pressure, $P_{SUPP} = 19$ kPa, the device oscillated with a period of 1.1 s, calculated from the average peak-to-peak distance in the plot of pressure versus time at one of the three outputs (Fig. 1C). The maximum output pressure (~14.5 kPa) was smaller than the supply pressure, P_{SUPP}, indicating that the pulldown resistor induced a pressure drop during oscillation in the same manner as it does during the switching of a single inverter. The minimum output pressure (~4 kPa) was slightly below P_{UNFOLD} of 6 kPa, but not at P_{ATM}, because the bladder starts to inflate immediately after the buckling-sheet inverter is unfolded (when pressure inside the bladder is still near P_{UNFOLD}; that is, the initial condition for Fig. 2A, state 1). We calculated the amplitude by subtracting the minimum pressure from the maximum pressure. Because of the pneumatic capacitance C (kg/kPa) from the internal air volume of the system, and the flow resistance R (kPa·s/kg) of the tubing, both inside and in between inverters, the pressure output of the inverters did not switch instantaneously, but instead gave rise to an oscillation with finite buckling and unfolding times.

Analytical model for BRO with controlled operational characteristics
We characterized the dependence of the period and the amplitude of the BRO on each of three adjustable system parameters: the supply pressure (P_{SUPP}), the pneumatic resistance from the pulldown resistor (R_{PULL}), and the interdevice pneumatic resistance (R_{TUBE}, associated with tubes connecting the buckling-sheet inverters). The two alternating states of the ring oscillator, i.e., buckling and unfolding of the connected buckling-sheet inverters, can be understood through an analogous electrical circuit (Fig. 2A), where each buckling or unfolding event can be modeled as a resistor-capacitor (RC) circuit with each capacitor-like bladder either charging or discharging, respectively. To derive expressions for the oscillation period and the amplitude as a function of P_{SUPP}, R_{PULL}, and R_{TUBE}, we modeled the airflow between two adjacent inverters in the same state of actuation. The buckling time (t_B) for one individual buckling-sheet inverter can be expressed as Eq. 1 (derivation in the Supplementary Materials and fig. S7)

$$t_B = R_{EFF} \times C_{BSA} \times \ln\left[\frac{(P_{EFF} - P_{UNFOLD})}{(P_{BUCK} - P_{EFF})}\right] \tag{1}$$

where C_{BSA} represents the intrinsic pneumatic capacitance from an individual BSA, defined as the rate of change of mass of fluid inside the BSA with respect to its internal pressure (1). C_{BSA} could be tuned by varying design parameters according to the scaling $C_{BSA} = f(d, EI)$, where d is the diameter of the pneumatic bladder and the product EI is the bending stiffness of the sheet itself, consisting of the elastic modulus of the sheet, E, and the area moment of inertia, I (which, in turn, is proportional to the cube of the thickness of the sheet, t^3); C_{BSA} increases with larger bladder diameters but decreases with stiffer sheets that resist deformation and expansion of the bladder.
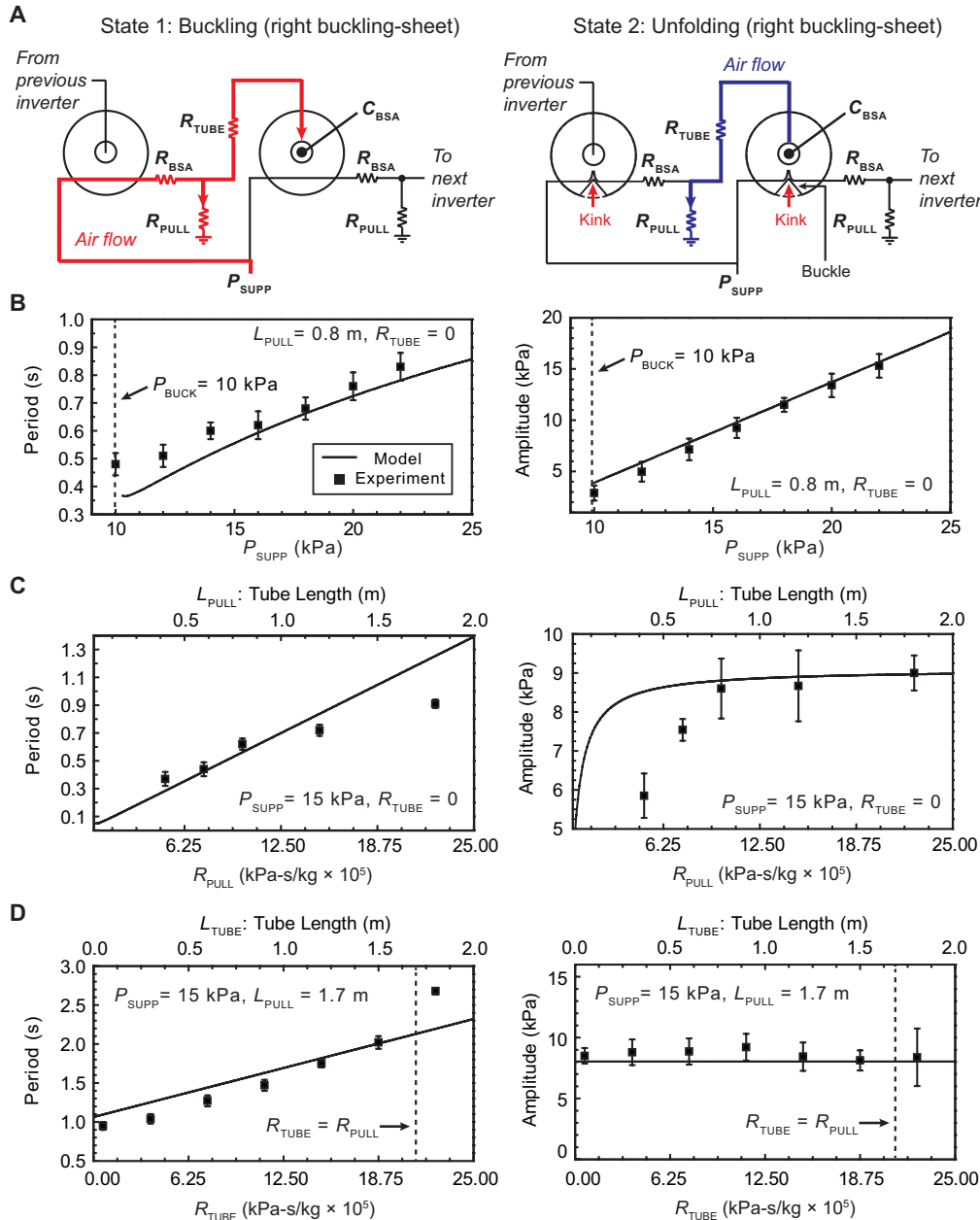
Fig. 2. Response to variable supply pressure and pneumatic resistances from pulldown resistor and interdevice resistor. The ring oscillator always contains either two adjacent unfolded buckling-sheet inverters with one inverter buckling (A; state 1) or two adjacent buckled inverters with one inverter unfolding (A; state 2). These two alternating states of each buckling-sheet inverter can be modeled using analogous RC circuits to estimate the overall period of a cycle during oscillation (A). We performed experimental parametric sweeps in oscillation period and amplitude over multiple supply pressures (B), pneumatic resistances resulting from pulldown resistors (C), and interdevice pneumatic resistors resulting from additional tubing connecting buckling-sheet inverters (D). Predictions from the analytical RC circuit model are overlaid as solid curves (B to D); note that the slight discrepancy between model and experiment is reasonable for modeling of flows of gases in small-diameter tubes, which often deviate from predictions by over 10% (*33*). Error bars in (B) to (D) represent the SD of the oscillation period and amplitude (with corresponding supply pressure and pneumatic resistances) from 10 measurements.

The effective pressure of the system, $P_{EFF} = (P_{SUPP} R_{PULL} + P_{ATM} R_{BSA})/(R_{PULL} + R_{BSA})$, captures the contributions of both the atmospheric and supply pressures, and the effective pneumatic resistance of the circuit, $R_{EFF} = (R_{TUBE} R_{BSA} + R_{PULL} R_{BSA} + R_{PULL} R_{TUBE})/$

$(R_{PULL} + R_{BSA})$, accounts for contributions from the three relevant pneumatic resistances: (i) the pulldown resistor (R_{PULL}), (ii) the interdevice pneumatic resistance (R_{TUBE}), and (iii) the pneumatic resistance of the flow-control tubing on the BSA (R_{BSA}). The pneumatic resistances can be tuned by changing the length and inner diameter of tubing based on the fluid mechanics of an internal flow (Supplementary Materials). Similarly, the unfolding time (t_U) of a buckling-sheet inverter can be expressed as Eq. 2 (derivation in the Supplementary Materials and fig. S7)

$$t_U = R_{EFF}^* \times C_{BSA} \times \ln\left[\frac{(P_{EFF} - P_{ATM})}{(P_{UNFOLD} - P_{ATM})}\right] \quad (2)$$

where $R_{EFF}^* = R_{TUBE} + R_{PULL}$ is a simplified form of R_{EFF} corresponding to the unfolding RC circuit, in which R_{BSA} approaches infinity due to the kinking of the flow-control tube. The resulting equation for the total oscillation period (t_{PERIOD}) of a ring oscillator containing n buckling-sheet inverters is therefore given by Eq. 3, where t_B is the buckling time and t_U is the unfolding time

$$t_{PERIOD} = n \times (t_B + t_U) \quad (3)$$

In addition, we derived an analytical expression for the pressure amplitude (A) during oscillation as $A = P_{EFF} - P_{UNFOLD}$ (derivation in the Supplementary Materials).

As P_{SUPP} was increased from 10 kPa (P_{BUCK}) to 22 kPa, the oscillation period (t_{PERIOD}) increased from 0.5 to 0.8 s for the case where R_{TUBE} is negligible (Fig. 2B). This behavior is explained by Eq. 2 and eq. S5, where t_U grew logarithmically with P_{SUPP}, making P_{SUPP} the dominant factor to increase t_{PERIOD}. Conversely, when R_{TUBE} is large (comparable with R_{PULL}), the oscillation period, t_{PERIOD}, decreases as the supply pressure, P_{SUPP}, increases (when P_{SUPP} is small, i.e., <13 kPa) (fig. S8); these contrasting regimes, captured here in our analytical model according to the analogous behavior in electrical systems (*32*), have not been observed or described in prior work on pneumatic devices. The oscillating pressure amplitude at each output

was increased from 3 to 15 kPa as P_{SUPP} increased for the case where R_{TUBE} is negligible. Considering that P_{UNFOLD} is the same regardless of P_{SUPP}, the amplitude A is linearly proportional to P_{SUPP} (as dictated by eq. S5 and eq. S12).

The pulldown resistors (with pneumatic resistance R_{PULL}) are also critical components in controlling the oscillation behavior (Fig. 2C). The pneumatic resistance can be represented by a length of tubing (L) with a known inner diameter. The total oscillation period t_{PERIOD} was linearly proportional to R_{PULL} because the rate of airflow through the pulldown resistor to the atmosphere decreases as L increases. This enhances the "effective" P_{SUPP} from the previous inverter to the next one and results in a larger t_U. As R_{PULL} increases above a threshold value of 0.75 m, the amplitude A starts to saturate. Equations S5 and S12 show that A will reach the value $P_{SUPP} - P_{UNFOLD}$ if the length of tubing is infinite. The slight discrepancies between model predictions and experimental results for R_{PULL} versus t_{PERIOD} and R_{PULL} versus A are reasonable for modeling of flows of gases in small-diameter tubes, which often deviate from predictions by over 10% (*33*). The error may also result from comparison of our analytical model from first principles with a nonideal real-world system. We found that we can achieve independent control over t_{PERIOD} with the same A by changing R_{TUBE} as another design factor for oscillation (Fig. 2D). Both the model and experimental data confirm that a BRO can access a wide range of periods of oscillation, from below 1 s to many seconds (theoretically from 0.1 s to an infinite period).

Electronics-free, intrinsic locomotion of a BRO

A BRO can achieve undulating locomotion because the constituent buckling-sheet inverters generate translational motion during folding and unfolding (Fig. 3). Each buckling-sheet inverter generates this locomotion by leveraging anisotropic friction designed into the system (*4, 10, 13*) due to asymmetric buckling. In more detail, if a single BSA contacts a flat surface for straightforward motion, only two points at the edges of the conical sheet meet the surface, while the rest of the structure is not in contact with the surface (*26*). Although these two pseudo-feet with different contact angles can lead to a fore-aft frictional asymmetry leading to motion, a single-level locomotor can easily lose its balance. In contrast, the BRO has six contact points (two for each BSA) and exhibits stable and conformal locomotion, even on undulating and uneven surfaces such as mounded sand, without adding mechanical elements (discussed in the next section). To achieve collective motion from the system on a flat surface, we arranged three buckling-sheet inverters in a triangular configuration, attached to each other with a thin flexible sheet to form a BRO. We selected three control elements because at least three pneumatic inverters are required to generate a pneumatic ring oscillator with system-level instabilities such that we could achieve electronics-free locomotion. Rather than adding other pneumatic circuit elements and increasing system complexity, we changed the relative arrangement of the three (i.e., the smallest unit number to form a ring oscillator) buckling-sheet inverters such that we could program the resulting BROs for target motions using a single, constant pressure input. One advantage of
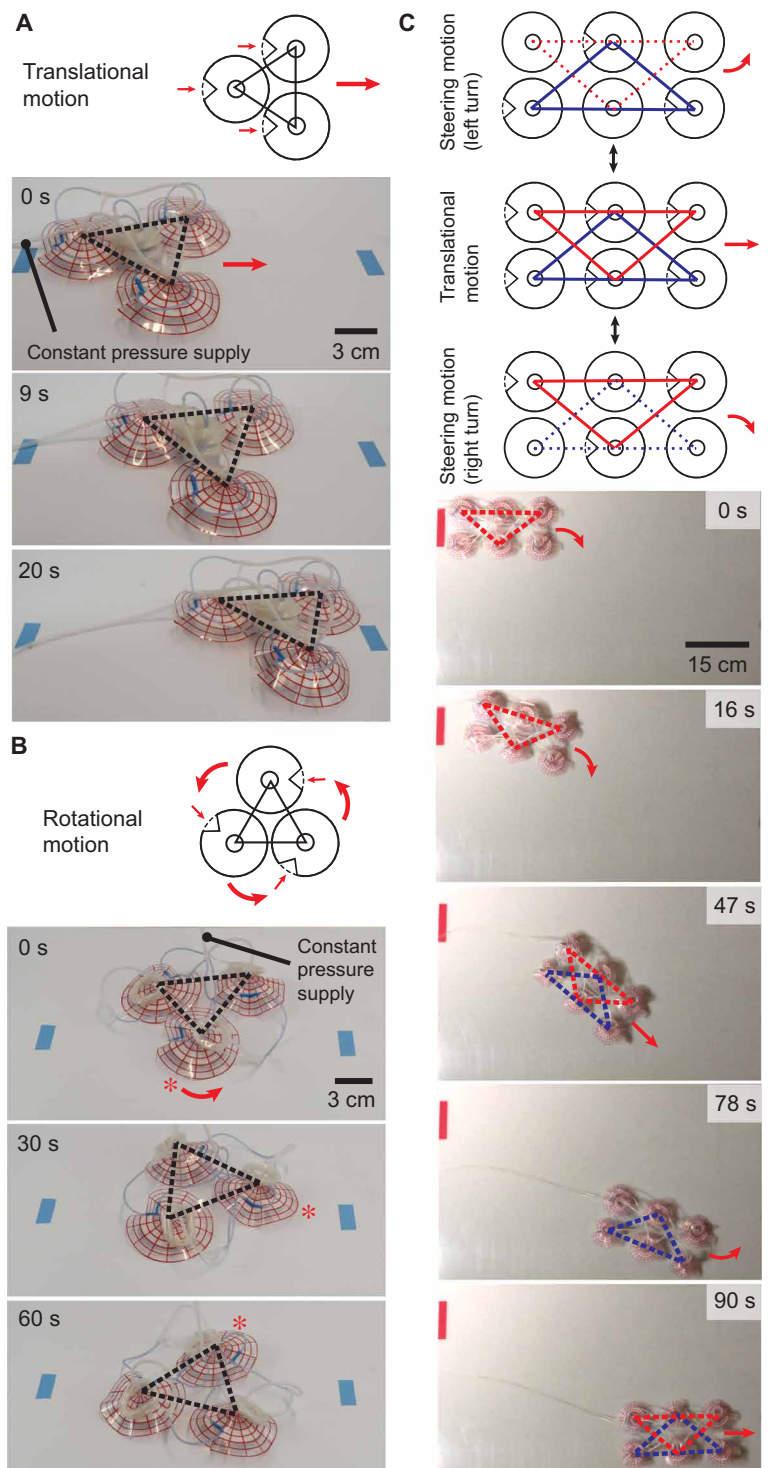

Fig. 3. Robot locomotion from BROs. BROs as a locomotive system can achieve both (**A**) translational (at 43 m/hour) and (**B**) rotational (at 0.45 rpm) motion, simply by changing the orientations of the buckling points on constituent buckling-sheet inverters. The three inverters in these oscillators were arranged in a triangular configuration to achieve collective motion. By integrating two BROs in a single robotic system, hybrid locomotion consisting of steering (both turning right and left) and translation was achieved by selectively applying two pneumatic inputs (**C**).

this approach is that we can reuse the unit buckling-sheet inverter as a single, repeated circuit element, for different applications, without redesigning additional components.

When the positions of the buckling points are aligned parallel to each other, a single, constant pressure supply (P_{SUPP}) of 20 kPa generates translational locomotion (Fig. 3A). The calculated oscillation period and amplitude of internal pressure from the analytical models were 1.0 s and 13 kPa, respectively (with the design parameters of L_{PULL} = 0.8 m and L_{TUBE} = 0.08 m); meanwhile, the measured period from the video (movie S3) was about 1.1 s, in agreement with the model. On a smooth surface of plastic (styrene) as a terrain, the BRO traveled at an average velocity of 12 mm/s (~43 m/hour). This speed of translational motion (~0.03 body lengths per second) on a flat surface is faster than that of the locomotor system based on a single bistable valve under a supply pressure of 17 kPa [~0.01 body lengths per second, (3)] because of the higher rate of oscillation from the BRO. Considering the similar levels of input pressure used to operate these two robotic systems (i.e., the BRO and the locomotor based on a bistable valve), the ability of the BRO to convert compressed air at a given pressure to speed of movement is superior. Using the same design parameters, the BRO demonstrated rotational locomotion by changing the arrangement of the buckling positions of the three BSAs (Fig. 3B). Here, the buckling positions within the same triangular system were arranged such that they were rotationally offset from each other by 120°. With P_{SUPP} of 25 kPa, this configuration of a BRO achieved a rotational speed of about 2.7°/s (~0.45 rpm) on the same terrain (movie S4). The estimated oscillation period and amplitude from the model were 1.2 s and 19 kPa, respectively.

By integrating two BROs together, we achieved both translational motion and steering (i.e., turning to the left and right), using a single robotic design, controlled by two pneumatic inputs (Fig. 3C and movie S5); this selective mode of locomotion from the twinned BRO with six buckling-sheet inverters is not possible with a single BRO consisting only of three inverters. The two BROs in a triangular configuration were assembled as two isosceles triangles, each forming an independent pneumatic oscillator, or ring. The two BROs were aligned such that their bases were parallel, with the apex of each BRO bisecting the base of the opposing BRO. All the buckling orientations were aligned parallel to each other. By applying pressure to both of the BROs simultaneously, the robot translates forwards, whereas it steers to the left or right by applying pressure to just one BRO (Fig. 3C). In this manner, we demonstrated hybrid locomotion in-plane with multiple translational and steering motions by selectively operating two independent rings in the robot (Fig. 3C). First, the robot turned right by applying pressure (25 kPa) to the first BRO (the ring with an inverted triangle colored with red) such that it steered rightward by ~45° in 32 s. By applying the same pressure input to the second BRO (the ring with a triangle colored with blue) simultaneously, the robot translated forward at a speed of 10 mm/s (~36 m/hour). The twinned BRO, however, is slightly slower than a single BRO, probably because the phase difference between the two constituent oscillators had a minor effect on the net motion. Turning the first BRO off (so that only the second BRO is pressurized) induced steering to the left by ~45° in 35 s. We then applied pressure to both of the BROs so that the robot moved forward in a straight line. The oscillation period of each ring was ~0.8 s from both the experiment and model. We designed and modeled the twinned BROs with L_{PULL} of 0.4 m and L_{TUBE} of 0.08 m.

Tethered and untethered locomotion across multiple terrains

A BRO can exhibit undulating and conformal locomotion across compliant surfaces with different rheologies, and also interfaces, including mounded sand (which we call "sand dunes") and a water surface, without changing the original design (Fig. 4, A and B). Such multimodal robot movements were possible on multiple terrains beyond smooth terrestrial surfaces because the BRO is lightweight (<16 g), and the actuation dynamics of the BRO are temporally asymmetric ($t_U \neq t_B$) such that the system can generate a net positive impulse on the terrain. For locomotion over sand (a medium with high, nonlinear, apparent viscosity), we applied a supply pressure P_{SUPP} of 60 kPa (with the same design parameters for the BROs in Fig. 3A, i.e., L_{PULL} = 0.8 m and L_{TUBE} = 0.08 m), where the calculated oscillation period and amplitude are 1.7 s and 48 kPa, respectively. The experimentally observed period (~2 s) obtained from the video (movie S6) matches that of the model. The average speed of locomotion was about 0.7 mm/s (~2.5 m/hour) (Fig. 4A). The BRO moves forward along sand dunes with uneven surface topographies when each constituent buckling-sheet inverter unfolds. This conformal motion of the system-level locomotor is possible without support from mechanical components [which would require extra fabrication and assembly processes with increasing system complexity (3)] because, even if one of constituent BSAs loses its balance or contact with the terrain, the other devices in the system can still achieve forward motion not attainable by a single BSA.

On the water surface, however, a BRO (with the same design parameters of L_{PULL} = 0.8 m and L_{TUBE} = 0.08 m) can swim with a much lower supply pressure, P_{SUPP}, of 15 kPa. With the smaller period of 0.74 s and a lower amplitude of 9 kPa calculated from the model, the BRO moved with an average locomotion speed of about 7.2 mm/s (~25.7 m/hour), 10 times faster than on the sand (Fig. 4B). The period measured from the video was ~0.7 s, in agreement with the value from the model (movie S7). In contrast to the movement on sand, the constituent buckling-sheet inverters propel the system (i.e., the BRO) when they buckle, not when they unfold. Consequently, the locomotion direction during swimming was opposite to the direction on sand as the fold on each of the buckling-sheets is a "pusher" on sand and a "puller" in water. Furthermore, by integrating a BRO with an onboard pneumatic source, we demonstrated untethered robot locomotion (Fig. 4C and movie S8). The untethered BRO enables operation of a low-profile, lightweight soft robot without the need for added actuators or limbs, or for complicated control hardware (like solenoid valves). It achieved translational locomotion on a pool table with an average speed of 2 mm/s (~7 m/hour) (Fig. 4D). The oscillation period and amplitude predicted by the analytical model were 1.6 s and 33 kPa, respectively, in agreement with the measured oscillation period observed from the video (movie S8), which was 1.5 s. Considering that the total weight of the untethered source (28 g) is much heavier than the weight of the BRO itself (6 g)—that is, a load of over 4× body weight—the BRO exhibits a notable ability to carry loads.

The beam-climbing robot from a BRO

By supplementing a BRO with additional BSAs to enhance motion, we created a beam-climbing robot that operates with only a single, constant-pressure input (Fig. 5 and figs. S9 and S10). The beam-climbing robot combines anisotropic friction, built into its feet, with undulations induced by the BRO to climb along an upwardly
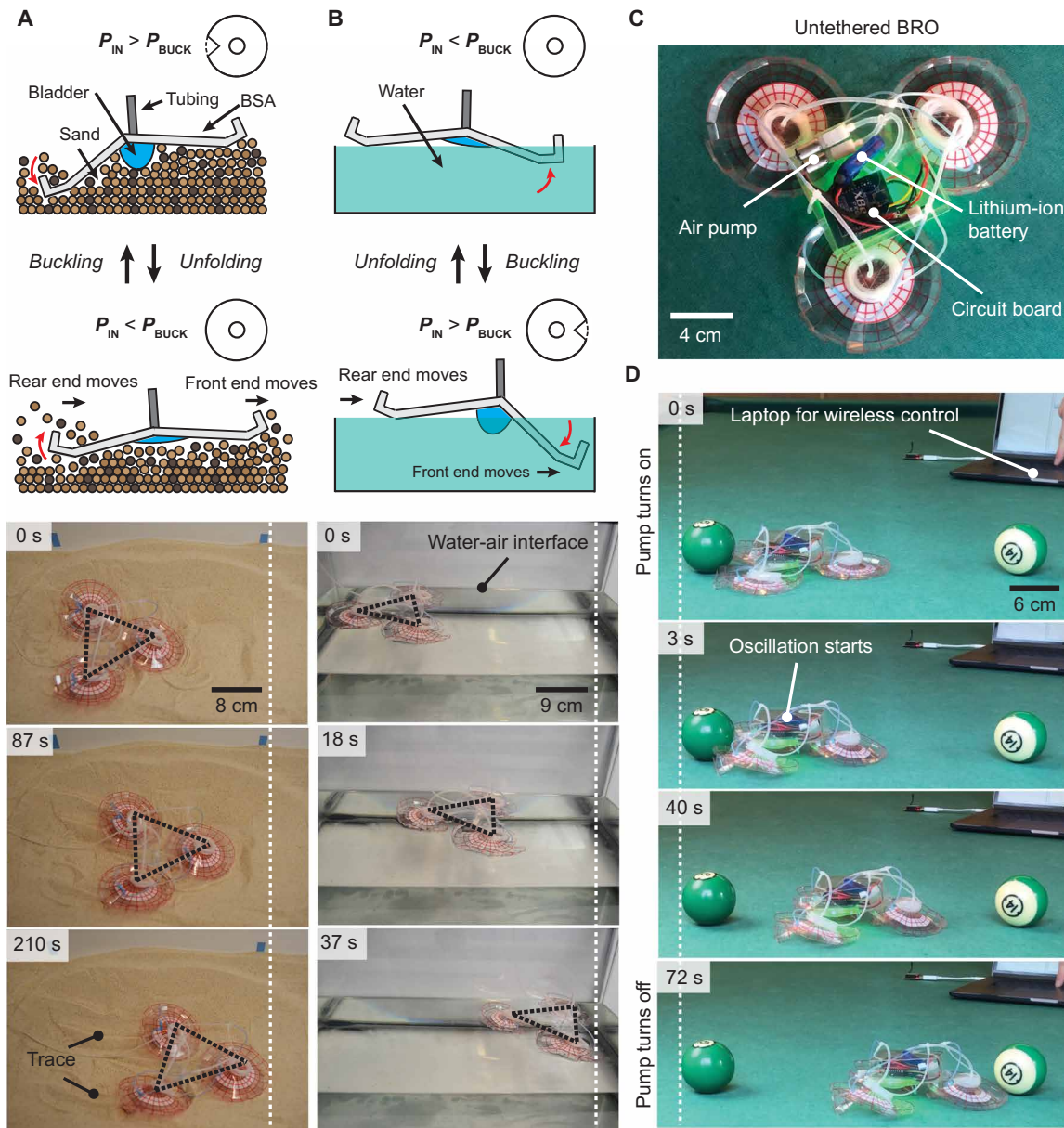
Fig. 4. Tethered and untethered robot movements from BROs across multiple terrains. BROs can achieve robot locomotion on compliant media such as a sand dune (~2.5 m/hour) (**A**) and a water-air interface (~25.7 m/hour) (**B**). By integrating a BRO with an onboard pneumatic source (**C**), untethered locomotion on a pool table (i.e., on the surface of cloth) with an average speed of ~7 m/hour was achieved (**D**). The edges (edge width of 1 cm) of the buckling sheets were manually folded with a "turned-up" shape to prevent accumulation of sand in (A) and to balance the weight of the BRO with buoyancy in (B).

inclined beam (Fig. 5A and fig. S11). Each BSA in the BRO is fixed to a semi-soft (styrene) frame, and the tubing leading to the bladder of each buckling-sheet inverter is connected to two additional BSAs such that they oscillate in tandem with that inverter. The additional actuators connect two styrene frames such that the frames are pulled together when the actuators buckle and are pushed apart as they unfold. The styrene frames support the robot and grip the beam on two opposing sides with silicone rubber feet that contact the beam at a 45° angle. The angle of the feet creates anisotropy in friction in the direction of the beam, making it easier to push the frame in one direction than the other, so, rather than stationary undulation, the robot climbs along the beam as the BRO oscillates.

The beam-climbing robot translated along the beam even when the beam was oriented vertically. The speed of the out-of-plane locomotion was 3.1 mm/s (~11 m/hour), 2.2 mm/s (~8 m/hour), and 1.5 mm/s (~6 m/hour) when the beam was tilted at 0° (horizontal), 45°, and 90° (vertical), respectively (Fig. 5, B to D, and movies S9 to S11). To achieve the climbing motion, we supplied P_{SUPP} of ~50 kPa. Under the given conditions of pneumatic components, the period of oscillation of the climber was about three times larger than the BRO without additional actuators because of a threefold increase in pneumatic capacitance. Adding extra pneumatic capacitance in parallel to only one inverter of the BRO would cause the period of the oscillation to be larger, resulting in an irregular
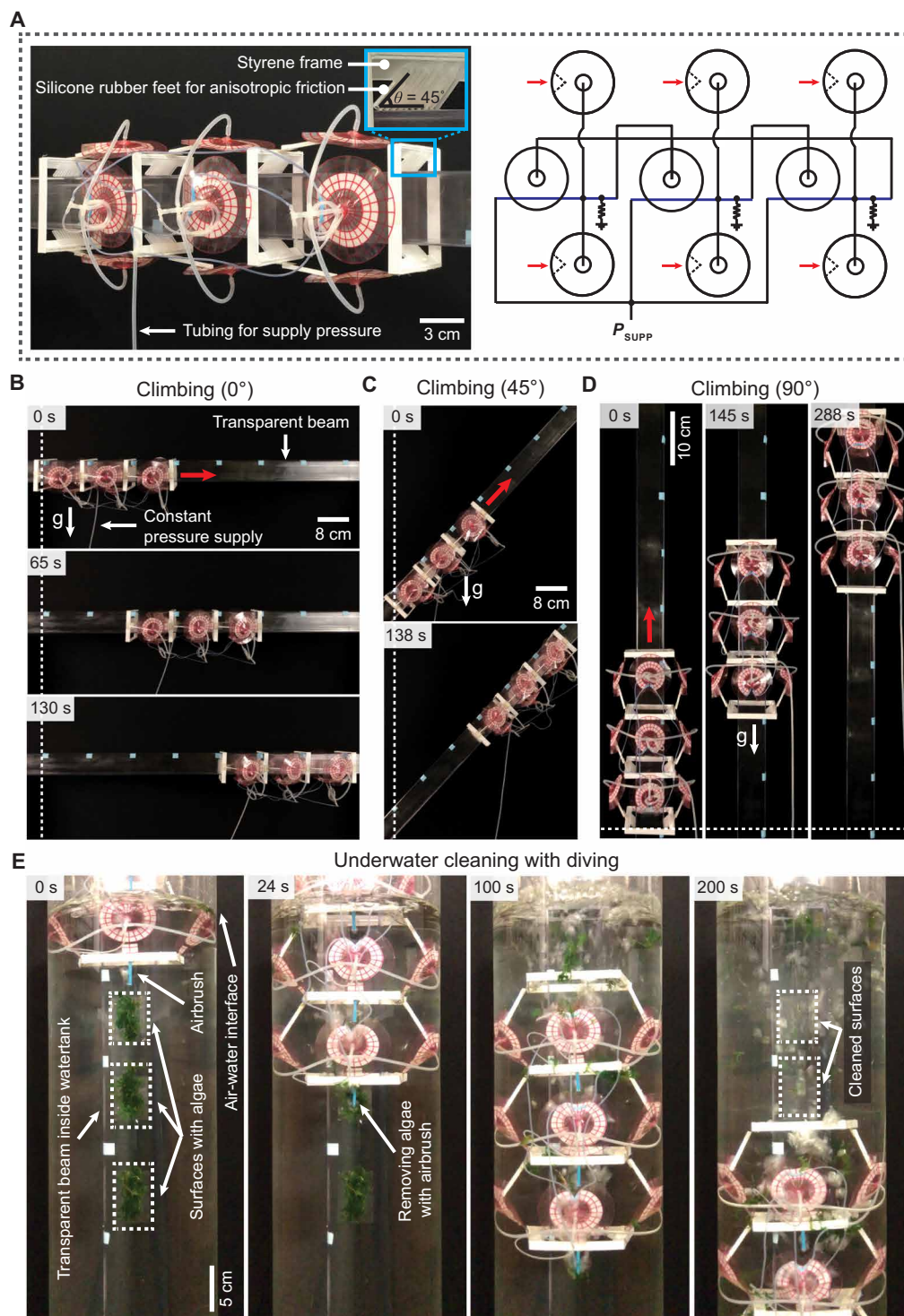
Fig. 5. The beam-climber robot, using a BRO. The beam-climber robot was fabricated by supplementing a BRO with two additional BSAs and a pair of semi-soft feet per each buckling-sheet inverter (**A**). The robot achieved climbing motion with a speed of ~11 m/hour along a horizontal direction (**B**), ~8 m/hour with 45° tilting of the beam (**C**), and ~6 m/hour upward in the vertical direction (**D**). The beam climber can also dive underwater against its own buoyancy with the average speed of ~12 m/hour and perform underwater cleaning with airbrushes (powered by recovering and redirecting the flow of air that travels through the pulldown resistors during normal locomotion) attached to the robot (**E**).

temporal oscillation profile, and potentially opening applications in pneumatic timing circuits, or unique new modes of locomotion. The measured and calculated oscillation periods were both ~1.7 s. The beam climber can also traverse underwater with an average speed of 3.5 mm/s (~12 m/hour), even against its own buoyancy (it experiences a significant buoyant force because it is filled with air) (Fig. 5E and movie S12) with an input pressure of ~70 kPa and a corresponding period of ~1.7 s. Here, we approximated the buoyant force ($F_B = -\rho g V$) by measuring the volume of the bladder attached on the buckling-sheet inverter (~3 ml) when we applied P_{BUCK}. Because the beam climber consists of nine buckling-sheet inverters, the total volume of the air oscillating inside the robot system is about $V \sim 27$ ml, giving rise to $F_B = 0.3$ N, where the density of water, ρ, is ~1000 kg/m³. By increasing the level of P_{IN} to keep the difference between P_{ATM} and P_{IN} at ~70 kPa, deep-sea operation could be achieved.

The beam climber can clean algae and other biofouling contaminants from underwater beams or pilings. We demonstrated that the beam climber can dive underwater and remove artificial algae attached to the surface of a beam with soft airbrushes attached to the body of the robot (Fig. 5E). These airbrushes were powered by recovering and redirecting the exhaust air that already flows from the pulldown resistors during normal operation, driven by the pressure drop from the internal bladders on each buckling-sheet inverter to the aquatic environment (i.e., underwater) during oscillation. In this manner, the beam climber can clean underwater surfaces while simultaneously climbing downward along a beam, using only a single, constant supply of pressure as its input.

DISCUSSION

Locomotion of soft robots currently relies primarily on pneumatic actuators that must be inflated and

deflated in a coordinated manner (5). Soft pneumatic oscillators provide an alternative to electronic oscillators to achieve this behavior because they simultaneously provide the actuation forces to change the spatial morphology required for locomotion while also generating the temporal pattern to coordinate the motion, reducing the overall complexity of the control required to generate and coordinate the complex movements required for locomotion. Soft devices capable of such behavior shown in prior work have suffered from drawbacks, though: They either have been constrained to low rates of airflow (limiting speed) (22) or have required complex fabrication processes (limiting widespread adoption) (1–3). To overcome these issues and enable simple control of the locomotion of soft robots, we developed the BRO, fabricated from flexible, but inextensible, sheets. The BRO relies on three instabilities: the out-of-plane buckling of the sheets (29, 30) building on our prior work on this mode of locomotion (26), the subsequent kinking of pneumatic tubing attached to the sheets (34), and the system-level instability of three buckling-sheet pneumatic inverters (each of which is composed of a buckling sheet and kinking tube) connected in a loop.

The BRO is able to generate motion directly from its own interaction with its surroundings, and thereby offers intrinsic scalability—the speed of locomotion can be increased or decreased based on the design of the BRO because the speed is directly proportional to the size of the BRO. Recently, we have developed a scaling law to show that the speed of a BSA is linearly proportional to the diameter of the sheet (26). This relationship means that, if we increase the diameter to 2 m, theoretically, the resulting speed of a single BRO could be ~19 m/min (and ~16 m/min for a twinned BRO). With this scalability in mind, large untethered BROs at the size scale of humans can, in principle, be deployed to transport people and goods in factories or warehouses. In addition, the speed is also proportional to the frequency of the actuation; considering that the oscillation period (or frequency) of the BRO is widely tunable by changing pneumatic components, with system optimization of the scalable BRO, we believe we can further increase the speed fast enough to support real-world applications (35, 36). The ability of the BRO to traverse a variety of terrains also promises use in application spaces ranging from undersea robotics (as indicated by the BRO's ability to clean algae from underwater beams) to exploration of dusty environments such as deserts, where the BRO can use its ability to traverse granular media.

The buckling-sheet inverter and the BRO can also be used to control other types of actuators within integrated robot systems. As we demonstrated in Fig. 5, the BRO can control separate actuators—in this case, additional BSAs combined with styrene frames—to realize beam climbing motions with the entire robotic system. On the basis of these experimental results, we believe that the buckling-sheet inverter and BRO will be able to control many different types of soft pneumatic actuators with an operational pressure range between 0 and 80 kPa (80 kPa is the upper pressure limit that the buckling-sheet inverter can control without system failure). In particular, the BRO as a pneumatic controller may be critical for use in robotic systems that require fast actuation; the BRO can control multiple oscillatory pressure outputs with oscillation periods as small as 0.1 s (i.e., 10 Hz). Considering the volume of the air and the pressure range (large enough to actuate mesoscale pneumatic actuators) controlled by the BRO, the speed of the oscillation is remarkable and is much faster than the pneumatic ring oscillator based on bistable valves shown in prior work, which could only reach a minimum oscillation period of greater than 5 s (i.e., 0.2 Hz) (1).

Using only low-cost, commercially available materials assembled in a simple stacking process, the BRO converts a constant input pressure to coordinated, oscillating output pressures at flow rates appropriate for actuation of soft robots. The BRO is capable of both linear translational and rotational motion over varied terrain, even without a tether, and can climb upward against the force of its own weight—or downward against buoyant force when underwater—with the capability for underwater cleaning of surfaces, as demonstrated in this work. This simple platform represents a step toward the mass production and deployment of untethered soft robots capable of complex locomotion, but without the requirement for complicated control systems, in homes, workplaces, and potentially even dangerous environments like the deep sea.

MATERIALS AND METHODS
Research objectives and design
This study was designed to demonstrate an approach to enable both tethered and untethered locomotion across varied terrains driven by the oscillatory internal pressure of the BRO and to highlight that this robotic oscillator can autonomously generate complex locomotion and behaviors using only one input held at a constant pressure. We also characterized the BRO experimentally, with parametric sweeps performed over the relevant pneumatic system (supply pressure and pneumatic resistances) for validation of the analytical model developed in this work. We fabricated all of the components of the soft robotic systems using commercially available materials without relying on complex fabrication processes, and thus reduced barriers to reproduction and widespread adoption of this type of design.

Fabrication of BSA, pneumatic inverter, and BRO
Each BSA was fabricated from a circular sheet of polycellulose acetate (an overhead transparency sheet). We attached a thin circular nylon film with a diameter of 4 cm to the center of the sheet using double-sided tape manually cut with a ring-shape (inner and outer diameters of the ring were 2 and 4 cm, respectively) to form a bladder (diameter of 2 cm when flat). Thin polydimethylsiloxane tubing connects the bladder to a pneumatic source, and the connection was sealed with a hot-melt adhesive [Surebonder Glue Sticks, poly(amidoamine)] using a glue gun. The transparency sheet and the bladder are both flexible but inextensible. Upon the first actuation, the initial buckling instability created in the sheet occurs at a random position along the radial direction. This buckle can be directed by hand to the desired position. To fabricate a pneumatic inverter from the buckling sheet, we attached a pneumatic flow-control tube on the surface of buckling sheet across the buckling position. Details specific to the fabrication of the BSA and pneumatic inverter are presented in the Supplementary Materials. Last, each BRO was assembled from three buckling-sheet inverters by connecting the output of each inverter to the input of the next inverter in a loop, or ring.

Preparation of untethered BRO
We prepared the untethered BRO using an onboard pneumatic pressure supply controlled and powered by a microcontroller (Microchip, ATMEGA168PA), two MOSFETs (ON Semiconductor NTZD3154NT; "ON Semiconductor" is the brand name of MOSFET), a WiFi-enabled communication chip (XBee, PRO S1), a voltage regulator (Microchip, MIC5219), and a 7-V rechargeable lithium-ion battery (Turnigy, 7.4 V, 300 mAh). This circuit controls two micropumps

that are connected in series (to increase total pressure) and was custom-made to minimize the weight and size of the robot. The control circuitry can be wirelessly controlled via IEEE 802.11 connectivity (WiFi). We used this setup to control the pneumatic pump of the robot wirelessly for on/off switching (schematic included in fig. S12).

Fabrication of beam-climber robot
We fabricated semi-soft styrene frames by laser cutting (Universal Laser Systems Inc., VLS 6.60 with a 60-watt CO_2 laser) styrene sheets with a thickness of 0.1 mm (Hygloss Products Inc., overhead projector transparency sheets made from cellulose diacetate) and attaching silicone rubber feet using super glue (Elmer's Products Inc., Krazy Glue) to generate anisotropic friction along the transparent plastic beam. We then attached the edges of each BSA in the BRO to the frame using doubled-sided tape (3M 9589 double-sided tape) and connected the additional BSAs between two styrene frames. Details specific to the materials and the fabrication of the beam-climber robot with multiple BSAs are presented in the Supplementary Materials.

Characterization of a pneumatic inverter based on BSA
We characterized the output pressure of a single buckling-sheet inverter as a function of the input pressure. We varied input pressure with a voltage-controlled electropneumatic regulator (SMC Pneumatics, ITV 0010-2BL) interfaced to a computer, where we characterized and recorded input, output, and supply pressures with electronic pressure sensors (Panasonic, ADP5151) connected to a data acquisition device (NI USB-6218 BNC). The supply pressure was set using a manual pressure regulator (Watts 03904). The input pressure was increased linearly from 0 to 15 kPa over 60 s and then decreased linearly back to 0 kPa over 60 s using the electropneumatic regulator.

Characterization of the BRO
During operation of the ring oscillator, three electronic pressure sensors (Panasonic, ADP5151) were attached to the connections between each of the inverters to measure the output pressures P_A, P_B, and P_C corresponding to each inverter in the BRO. The supply pressure, P_{SUPP}, was regulated by a manual pressure regulator (Watts, 03904) and was recorded with a fourth electronic pressure sensor of the same type (Panasonic, ADP5151). The amplitude and period of oscillation were determined by postprocessing the data.

SUPPLEMENTARY MATERIALS
www.science.org/doi/10.1126/scirobotics.abg5812
Materials and Methods
Supplementary Text
Figs. S1 to S13
Tables S1 and S2
Movies S1 to S12
References (37–40)

REFERENCES AND NOTES
1. D. J. Preston, H. J. Jiang, V. Sanchez, P. Rothemund, J. Rawson, M. P. Nemitz, W.-K. Lee, Z. Suo, C. J. Walsh, G. M. Whitesides, A soft ring oscillator. *Sci. Robot.* **4**, eaaw5496 (2019).
2. D. J. Preston, P. Rothemund, H. J. Jiang, M. P. Nemitz, J. Rawson, Z. Suo, G. M. Whitesides, Digital logic for soft devices. *Proc. Natl. Acad. Sci. U.S.A.* **116**, 7750–7759 (2019).
3. P. Rothemund, A. Ainla, L. Belding, D. J. Preston, S. Kurihara, Z. Suo, G. M. Whitesides, A soft, bistable valve for autonomous control of soft actuators. *Sci. Robot.* **3**, 7986 (2018).
4. D. Rus, M. T. Tolley, Design, fabrication and control of soft robots. *Nature* **521**, 467–475 (2015).
5. G. M. Whitesides, Soft robotics. *Proc. Natl. Acad. Sci. U.S.A.* **57**, 4258–4273 (2018).
6. M. T. Tolley, R. F. Shepherd, B. Mosadegh, K. C. Galloway, M. Wehner, M. Karpelson, R. J. Wood, G. M. Whitesides, A resilient, untethered soft robot. *Soft Robot.* **1**, 213–223 (2014).
7. B. Mosadegh, A. D. Mazzeo, R. F. Shepherd, S. A. Morin, U. Gupta, I. Z. Sani, D. Lai, S. Takayama, G. M. Whitesides, Control of soft machines using actuators operated by a braille display. *Lab Chip* **14**, 189–199 (2014).
8. R. F. Shepherd, F. Ilievski, W. Choi, S. A. Morin, A. A. Stokes, A. D. Mazzeo, X. Chen, M. Wang, G. M. Whitesides, Multigait soft robot. *Proc. Natl. Acad. Sci. U.S.A.* **108**, 20400–20403 (2011).
9. M. S. Verma, A. Ainla, D. Yang, D. Harburg, G. M. Whitesides, A soft tube-climbing robot. *Soft Robot.* **5**, 133–137 (2017).
10. Y. Matia, T. Elimelech, A. D. Gat, Leveraging internal viscous flow to extend the capabilities of beam-shaped soft robotic actuators. *Soft Robot.* **4**, 126–134 (2017).
11. C. C. Futran, S. Ceron, B. C. MacMurray, R. F. Shepherd, K. H. Petersen, Leveraging fluid resistance in soft robots, in *2018 IEEE International Conference on Soft Robotics (Robosoft)* (IEEE, 2018), pp. 473–478.
12. G. Gu, J. Zou, R. Zhao, X. Zhao, X. Zhu, Soft wall-climbing robots. *Sci. Robot.* **3**, eaat2874 (2018).
13. F. Berlinger, M. Duduta, H. Gloria, D. Clarke, R. Nagpal, R. Wood, A modular dielectric elastomer actuator to drive miniature autonomous underwater vehicles, in *2018 IEEE International Conference on Robotics and Automation (ICRA)* (IEEE, 2018), pp. 3429–3435.
14. R. K. Katzschmann, J. DelPreto, R. MacCurdy, D. Rus, Exploration of underwater life with an acoustically controlled soft robotic fish. *Sci. Robot.* **3**, eaar3449 (2018).
15. S. D. de Rivaz, B. Goldberg, N. Doshi, K. Jayaram, J. Zhou, R. J. Wood, Inverted and vertical climbing of a quadrupedal microrobot using electroadhesion. *Sci. Robot.* **3**, eaau3038 (2018).
16. Y. Chen, N. Doshi, B. Goldberg, H. Wang, R. J. Wood, Controllable water surface to underwater transition through electrowetting in a hybrid terrestrial-aquatic microrobot. *Nat. Commun.* **9**, 2495 (2018).
17. E. Acome, S. K. Mitchell, T. G. Morrissey, M. B. Emmett, C. Benjamin, M. King, M. Radakovitz, C. Keplinger, Hydraulically amplified self-healing electrostatic actuators with muscle-like performance. *Science* **359**, 61–65 (2018).
18. N. Kellaris, V. Gopaluni Venkata, G. M. Smith, S. K. Mitchell, C. Keplinger, Peano-hasel actuators: Muscle-mimetic, electrohydraulic transducers that linearly contract on activation. *Sci. Robot.* **3**, eaar3276 (2018).
19. S. K. Mitchell, X. Wang, E. Acome, T. Martin, K. Ly, N. Kellaris, V. G. Venkata, C. Keplinger, An easy-to-implement toolkit to create versatile and high-performance HASEL actuators for untethered soft robots. *Adv. Sci.* **6**, 1900178 (2019).
20. P. N. Duncan, S. Ahrar, E. E. Hui, Scaling of pneumatic digital logic circuits. *Lab Chip* **15**, 1360–1365 (2015).
21. P. N. Duncan, T. V. Nguyen, E. E. Hui, Pneumatic oscillator circuits for timing and control of integrated microfluidics. *Proc. Natl. Acad. Sci. U.S.A.* **110**, 18104–18109 (2013).
22. M. Wehner, R. L. Truby, D. J. Fitzgerald, B. Mosadegh, G. M. Whitesides, J. A. Lewis, R. J. Wood, An integrated design and fabrication strategy for entirely soft, autonomous robots. *Nature* **536**, 451–455 (2016).
23. M. A. Unger, H.-P. Chou, T. Thorsen, A. Scherer, S. R. Quake, Monolithic microfabricated valves and pumps by multilayer soft lithography. *Science* **288**, 113–116 (2000).
24. T. Thorsen, S. J. Maerkl, S. R. Quake, Microfluidic large-scale integration. *Science* **298**, 580–584 (2002).
25. A. Groisman, M. Enzelberger, S. R. Quake, Microfluidic memory and control devices. *Science* **300**, 955–958 (2003).
26. A. Nagarkar, W. K. Lee, D. J. Preston, M. P. Nemitz, N. N. Deng, G. M. Whitesides, L. Mahadevan, Elastic-instability-enabled locomotion. *Proc. Natl. Acad. Sci. U.S.A.* **118**, e2013801118 (2021).
27. Z. E. Teoh, B. T. Phillips, K. P. Becker, G. Whittredge, J. C. Weaver, C. Hoberman, D. F. Gruber, R. J. Wood, Rotary-actuated folding polyhedrons for midwater investigation of delicate marine organisms. *Sci. Robot.* **3**, eaat5276 (2018).
28. Y. Wang, X. Yang, Y. Chen, D. K. Wainwright, C. P. Kenaley, Z. Gong, Z. Liu, H. Liu, J. Guan, T. Wang, J. C. Weaver, R. J. Wood, L. Wen, A biorobotic adhesive disc for underwater hitchhiking inspired by the remora suckerfish. *Sci. Robot.* **2**, eaan8072 (2017).
29. E. Cerda, S. Chaieb, F. Melo, L. Mahadevan, Conical dislocations in crumpling. *Nature* **401**, 46–49 (1999).
30. E. Cerda, L. Mahadevan, Conical surfaces and crescent singularities in crumpled sheets. *Phys. Rev. Lett.* **80**, 2358–2361 (1998).
31. R. P. Feynman, R. B. Leighton, M. Sands, The Feynman lectures on physics; vol. I. *Am. J. Phys.* **33**, 750–752 (1965).
32. P. Horowitz, W. Hill, *The Art of Electronics* (Cambridge Univ. Press, ed. 2, 1989), p. 1125.
33. T. A. Ganat, M. Hrairi, Gas–liquid two-phase upward flow through a vertical pipe: Influence of pressure drop on the measurement of fluid flow rate. *Energies* **11**, 2937 (2018).
34. K. Luo, P. Rothemund, G. M. Whitesides, Z. Suo, Soft kink valves. *J. Mech. Phys. Solids* **131**, 230–239 (2019).

35. D. Drotman, S. Jadhav, D. Sharp, C. Chan, M. T. Tolley, Electronics-free pneumatic circuits for controlling soft-legged robots. *Sci. Robot.* **6**, eaay2627 (2021).

36. A. Rajappan, B. Jumet, D. J. Preston, Pneumatic soft robots take a step toward autonomy. *Sci. Robot.* **6**, eabg6994 (2021).

37. C. T. Crowe, *Engineering Fluid Mechanics* (John Wiley & Sons, ed. 9, 2009).

38. J. M. Cimbala, Y. A. Cengel, *Essentials of Fluid Mechanics: Fundamentals and Applications* (McGraw-Hill, 2008), p. 324.

39. R. W. Ogden, *Non-Linear Elastic Deformations* (Dover Publications Inc., 1997).

40. J. N. Reddy, *An Introduction to the Finite Element Method* (Mcgraw-Hill series in mechanical engineering, McGraw-Hill Higher Education, ed. 3, 2006), p. xvi, 766 pp.

Science Robotics

A buckling-sheet ring oscillator for electronics-free, multimodal locomotion

Won-Kyu LeeDaniel J. PrestonMarkus P. NemitzAmit NagarkarArthur K. MacKeithBenjamin GorissenNikolaos VasiosVanessa SanchezKatia BertoldiL. MahadevanGeorge M. Whitesides

View the article online
https://www.science.org/doi/10.1126/scirobotics.abg5812
Permissions
https://www.science.org/help/reprints-and-permissions

Use of think article is subject to the Terms of service

Supplementary Materials for

A buckling-sheet ring oscillator for electronics-free, multimodal locomotion

Won-Kyu Lee *et al.*

Corresponding author: George M. Whitesides, gwhitesides@gmwgroup.harvard.edu

The PDF file includes:

Other Supplementary Material for this manuscript includes the following:

Materials and Methods

<u>Fabrication of buckling-sheet actuator and pneumatic inverter</u>

Each buckling-sheet actuator was fabricated from a circular sheet of polycellulose acetate (Hygloss Products, Inc. overhead projector transparency sheets made from cellulose diacetate) with a diameter of 7 cm (**Fig. S1**). We attached a thin circular Nylon film (McMaster-Carr Nylon film, 0.005mm thick), with a diameter of 4 cm, to the center of the circular sheet using double-sided tape (3M 9589 double-sided tape) to form a pneumatic bladder. Thin tubing (McMaster-Carr PDMS tubing, 0.5 mm internal diameter) allows the bladder to attach to an external pneumatic source; we sealed the connection between the tubing and the cellulose acetate sheet with a hot-melt adhesive (Surebonder Glue Sticks, poly(amidoamine)) applied with a hot glue gun (Surebonder GM-160 Glue Gun, 10-watt). The transparency sheet and the Nylon bladder are both flexible but inextensible. When the bladder is pressurized, it expands in volume but contracts in diameter (due to its inextensible nature in the applied pressure range), applying stress to the entire transparency sheet. The cellulose acetate sheet releases stress by buckling out-of-plane. Upon the first actuation, the initial buckling instability created in the sheet occurs at a random position along the radial direction. When this buckled sheet is kept in the buckled state for a minute, the material develops a "buckling memory." After this initial "programming" of the buckling position, the sheet always buckles reproducibly in the same location—it thus becomes a reliable actuator and could operate up to ~ 80 kPa without failure. We previously conducted a reliability test for the buckling-sheet actuators with cyclic actuation and confirmed that the devices are stable hundreds of cycles of pressurization and depressurization *(26)*. To fabricate a pneumatic transistor from the buckling sheet, we attached a pneumatic flow-control tube with

reversible kinking composed of soft blue tubing (Smooth-On Smooth-Sil 950, 2 cm length, 3 mm inner diameter) connected on either side to the same PDMS tubing used to connect to the bladder (**Fig. S1**). The flow-control tubing was attached on the surface of buckling sheet, across the buckling position. We then attached the pneumatic pulldown resistor—a length of PDMS tubing with a small (0.8 mm) inner diameter to provide a resistance to airflow (**Fig. S7**). The pulldown resistor is required to create an inverter from the buckling-sheet transistor described above; without the pulldown resistor, the output state would always remain at the supply pressure after the first actuation.

Nonlinear finite element model for pneumatic inverter based on the buckling-sheet actuator

Nonlinear finite element method (FEM) modeling was employed to analyze the working principles of the buckling-sheet inverter (*40*), using the commercially available software package Abaqus (Version 2019, Dassault Systèmes, 175 Wyman Street, Waltham, MA 02451, United States). The global behavior of the buckling-sheet actuator was modeled by decoupling the bending of the sheet actuator from the buckling of a pneumatic flow-control tubing (**Fig. S4A**). This decoupling is justified since the structural stiffness of the buckling-sheet actuator is orders of magnitude higher than that of the elastomeric flow-control tubing. As a first step, the deformation upon pressurizing the pneumatic bladder of the buckling-sheet actuator was modeled while tracking the displacement of the attachment points of the flow-control tubing (**Fig. S4B**, **Movie S1**). To fix the location of the buckle on the buckling-sheet actuator, an imperfection was introduced in the geometry that matched the initial plastic programming done on the physical prototypes. All materials where modeled using a Neo-Hookean material model (*39*), where material parameters were determined experimentally by performing uniaxial tensile tests. In more detail, tensile tests on the materials

that make up the buckling-sheet inverter were done using an Instron 5969 universal testing machine with a 500 N load cell. The initial dimensions of the material specimens were measured using a caliper, where for the length the distance between the clamps of the tensile machine was taken (**Table S1**). The data of these tensile tests are depicted in **Fig. S13**. A linear regression was performed on the tensile data to determine Young's moduli of the different materials with values: 2.13GPa (acetate sheet), 0.32GPa (double-sided tape), 2.35GPa (Nylon film).

In addition, a small amount of material damping (Rayleigh damping with a damping coefficient of 0.2) was introduced in the material definition of the software. The circular sheets of polycellulose acetate, double-sided tape, and nylon film composing a buckling-sheet actuator were individually meshed using, in total, approximately 30,000 8-node brick linear elements (Abaqus element code C3D8H) and tied together to ensure structural lamination. Due to symmetry conditions, only half of the structure needed to be modeled. As a second step, the output displacement of the attachment points was used as a driving parameter to axially deform the flow-control tube while tracking the cross-sectional deformation of the central part of the tube (**Fig. S4C**, **Movie S2**), which is the location at which the kink forms (*34*). The tube was meshed using, in total, approximately 60,000 8-node brick linear elements (Abaqus element code C3D8R), and a Neo-Hookean material model. The results of both analyses where combined to generate the global behavior of the buckling-sheet inverter, as **Fig. S4D** shows. This analysis illustrates that the difference in threshold pressures between folding and unfolding originates largely from the small hysteretic behavior of the buckling-sheet actuator, which is enlarged by the significant nonlinear response of the tube due to the buckling-loading condition (*34*).

Preparation of untethered pneumatic source with a wireless control

We integrated a BRO with an on-board pneumatic source consisting of two micropumps and supporting control electronics to enable untethered robot locomotion (**Fig. S12**). The control circuitry of the untethered BRO consists of: (i) a microcontroller (Microchip ATMEGA168PA), (ii) a MOSFET (ON Semiconductor NTZD3154NT), (iii) a WiFi chip (XBee PRO S1), (iv) a voltage regulator (Microchip MIC5219), and (v) a rechargeable lithium-ion battery (Turnigy 7.4V, 300 mAh, 45-90C). For the autonomous movement of our oscillating robot, we used two SKOOCOM SC3101PM diaphragm pumps in series (purchased from Alibaba) controlled by the circuit board. The maximum pressure of a single micropump is 300 mmHg. It can be operated by applying a DC voltage between 3 V to 6 V, with corresponding currents between 150 mA and 350 mA.

Design and assembly of the beam-climber robot

The beam climber robot was fabricated by connecting a BRO to an additional three pairs of buckling-sheet actuators and mounting these actuators to four semi-soft styrene frames that grip a beam with silicone feet (**Figs. S10** and **S11**). The three pairs of actuators connect the four frames, and each pair of actuators is controlled by a different output signal from the BRO, such that the forward pair, middle pair, and rear pair actuate separately but sequentially. As the BRO actuates each pair, the corresponding rear frame is pulled forward, and as each pair of actuators is depressurized, the actuators relax to their original length and push the corresponding front frame forward (**Fig. S12**). Motion along the beam can be achieved due to the anisotropic friction of the silicone feet, which contact the beam at a 45° angle. The styrene pieces (Plastruct Inc.,

white styrene plate, 12.1 × 7.1 × 0.18 inches) and acetate pieces (Hygloss Products, Inc., overhead projector sheet acetate transparency film) were cut to size using a laser cutter (Universal Laser Systems Inc., VLS 6.60 with a 60-Watt CO_2 laser) or scissors, and the robot is held together with double-sided tape (3M 9589 double-sided tape), super glue (Elmer's Products, Inc., Krazy Glue) and a hot-melt adhesive (Surebonder Glue Sticks, poly(amidoamine)) applied with a hot-glue gun (Surebonder GM-160 Glue Gun, 10-watt). The semi-soft styrene frame was fabricated by laser cutting individual parts and gluing them together with the super glue and hot glue as shown in **Fig. S10**. Specifically, the silicone rubber feet (bundles of PDMS tubes 0.8 mm diameter) were attached to lengths of styrene using super glue (**Fig. S10A**). Then we glued (with hot glue) these lengths of styrene-PDMS composite to form rectangular frames (also made of styrene) that held the feet such that they contacted the beam at a 45° angle. We used four of these frames for one robot. To enable actuation, three pairs of buckling sheet actuators were mounted between the four frames. We mounted each actuator to the frame in front of it using the double-sided tape and an acetate sheet. We mounted each actuator to the frame behind it by gluing (using super glue) a thin piece of styrene along the "programmed" buckling position and gluing an acetate sheet between that piece of styrene and the frame (**Fig. S10B**). Finally, we mounted the three buckling-sheet inverters of the BRO directly onto the front three frames using double-sided tape, and we connected the corresponding pairs of actuators to each output pressure signal from the BRO as shown in **Fig. S11A-B**.

Supplementary Text

Analytical model for a BRO based on an analogous electronic circuit

We characterized the dependence of the period and the amplitude of the BRO on each of three adjustable system parameters: the supply pressure (P_{SUPP}), the pneumatic resistance from the pulldown resistor (R_{PULL}), and the inter-device pneumatic resistance (resulting from tubes connecting the buckling-sheet inverters; R_{TUBE}). Because the tubing volume is much smaller than the internal volume of the bladder in the actuator, we neglected compressibility along the tubing. We estimated a Reynolds number of Re ~ 10-100 for the gas (air), a much smaller value than the critical Reynolds number Re ~ 2,300 for transition to turbulent flow (*37, 38*). In **Figs. 2C-D**, we therefore modeled and calculated R_{TUBE} (or R_{PULL}) with the Darcy–Weisbach equation (*38*) for laminar flow (Eq. S1):

$$R_{\text{TUBE}} \text{ (or } R_{\text{PULL}}) = \frac{\Delta P}{\dot{m}} = \frac{128 \mu L}{\pi \rho D^4} \tag{S1}$$

In Eq. S1, ΔP (kPa) is the pressure difference between the ends of the tubing, $\dot{m}$ (kg/s) the mass flow rate of air, μ (Pa-s) is the dynamic viscosity of air, ρ is the density of air at standard pressure and temperature, and D and L are the inner diameter and the length of the tubing. Meanwhile, the shape of the tubing and the volume of pneumatic bladder of the buckling-sheet inverter itself depend on its deformation during the oscillation consisting of cyclic buckling-unfolding states. We therefore determined the characteristic pneumatic resistance (R_{BSA}) and capacitance (C_{BSA}) of the buckling-sheet inverter by determining the best fit of the final equation to the experimental data with these quantities used as fitting parameters.

To derive an equation for the oscillation period as a function of P_{SUPP}, R_{PULL}, and R_{TUBE}, and the number of inverters in the ring n, we modeled the airflow between two adjacent inverters that are in the same state of actuation, during both buckling and unfolding (**Figs. S8A** and **S8B**,

respectively), and extended the result to the entire ring oscillator. The oscillation period of a BRO containing n inverters (t_{PERIOD}) is the sum of the buckling times (t_B) and unfolding times (t_U) of all n buckling-sheet inverters.

During buckling, air flows from the pressure supply (P_{SUPP}) through the resistor (R_{TUBE}) to the bladder of buckling-sheet inverter (C_{BSA}) and to the atmosphere (P_{ATM}) through the pulldown resistor (R_{PULL}) simultaneously (**Fig. S7A**). Equation S2 from the analogous electronic RC circuit describes the time-varying pressure $P(t)$ inside the bladder of the buckling-sheet inverter:

$$\frac{dP}{dt} = \frac{1}{R_{TUBE} \times C_{BSA}} \times (P_I - P(t)) \tag{S2}$$

where P_I is:

$$P_I = \left(\frac{1}{\frac{1}{R_{PULL}} + \frac{1}{R_{BSA}} + \frac{1}{R_{TUBE}}} \right) \times \left(\frac{P_{SUPP}}{R_{BSA}} + \frac{P_{ATM}}{R_{PULL}} + \frac{P(t)}{R_{TUBE}} \right) \tag{S3}$$

In Eq. (S2), dP/dt is the derivative of $P(t)$ with respect to time during the buckling, i.e., from unfolded state ($P(t)$ below P_{UNFOLD}) to buckled state ($P(t)$ above P_{BUCK}). Notably, the minimum output pressure was slightly below P_{UNFOLD}, not P_{ATM}, because the bladder starts to inflate right after the buckling-sheet inverter is unfolded (when pressure inside bladder is still near P_{UNFOLD}; initial condition for **Fig. S7A**, State 1). Solving the differential equation with the boundary condition of $P(t=0) = P_{UNFOLD}$ resulted in the solution of $P(t)$ summarized by Equation S4:

$$P(t) = (P_{\text{EFF}} - P_{\text{UNFOLD}}) \times exp\left(^{-t}/(R_{\text{EFF}} \times C_{\text{BSA}})\right) + P_{\text{EFF}} \tag{S4}$$

Where the effective pressure (P_{EFF}) of the system captures the contributions of both the

atmospheric and supply pressures, and the effective pneumatic resistance (R_{EFF}) of the circuit

accounts for contributions from the three relevant pneumatic resistances: (i) the pulldown

resistor, (ii) the inter-device pneumatic resistance, and (iii) the pneumatic resistance of the flow-

control tubing on a buckling-sheet actuator (R_{BSA} and C_{BSA} indicate the intrinsic pneumatic

resistance and capacitance from the individual buckling-sheet actuator (BSA), respectively):

$$P_{\text{EFF}} = \frac{P_{\text{SUPP}} \times R_{\text{PULL}} + P_{\text{ATM}} \times R_{\text{BSA}}}{R_{\text{PULL}} + R_{\text{BSA}}} \tag{S5}$$

$$R_{\text{EFF}} = \frac{R_{\text{TUBE}} \times R_{\text{BSA}} + R_{\text{PULL}} \times R_{\text{BSA}} + R_{\text{PULL}} \times R_{\text{TUBE}}}{R_{\text{PULL}} + R_{\text{BSA}}} \tag{S6}$$

By assuming that $P(t)$ increased to P_{BUCK} when $t = t_{\text{B}}$, and by using the boundary condition of

$P(t_{\text{B}}) = P_{\text{BUCK}}$, we can derive t_{B} in the form of Equation S7:

$$t_{\text{B}} = R_{\text{EFF}} \times C_{\text{BSA}} \times ln\left[\frac{(P_{\text{EFF}} - P_{\text{UNFOLD}})}{(P_{\text{BUCK}} - P_{\text{EFF}})}\right] \tag{S7}$$

During unfolding, air flows from the bladder of the buckling-sheet inverter (C_{BSA}) to the

atmosphere (P_{ATM}) through the pneumatic resistors (R_{TUBE} and R_{PULL}) (**Fig. S7B**). Equation S8

from the analogous electronic RC circuit describes the time varying pressure $P(t)$ inside the

bladder of the buckling-sheet inverter during unfolding:

$$\frac{dP}{dt} = \frac{1}{(R_{\text{TUBE}} + R_{\text{PULL}}) \times C_{\text{BSA}}} \times (P_{\text{ATM}} - P(t)) \qquad \text{(S8)}$$

By solving the Eq. (S8) with the boundary condition of $P(\text{t} \rightarrow \infty) = P_{\text{ATM}}$, we derived the solution shown in Equation S9 for $P(t)$:

$$P(t) = (P_{\text{EFF}} - P_{\text{ATM}}) \times exp\left[^{-t}/_{(R_{\text{EFF}}^* \times C_{\text{BSA}})}\right] + P_{\text{ATM}} \qquad \text{(S9)}$$

Where $R_{\text{EFF}}^* = R_{\text{TUBE}} + R_{\text{PULL}}$ is the simplified form of R_{EFF} for the unfolding RC circuit, when R_{BSA} is infinite due to the kinking of the flow-control tube.

By assuming that $P(t)$ decreased to P_{UNFOLD} when $t = t_{\text{U}}$ and using setting the boundary condition for the oscillation, $P(t_{\text{U}}) = P_{\text{UNFOLD}}$, we can derive t_{U} as Equation S10:

$$t_{\text{U}} = R_{\text{EFF}}^* \times C_{\text{BSA}} \times ln\left[\frac{(P_{\text{EFF}} - P_{\text{ATM}})}{(P_{\text{UNFOLD}} - P_{\text{ATM}})}\right] \qquad \text{(S10)}$$

The oscillation period of a BRO containing n buckling-sheet inverters is therefore the sum of the buckling times (t_{B}) and unfolding times (t_{U}) of all n inverters (Eq. (S11), which is Eq. (3) in the main text):

$$t_{\text{PERIOD}} = n \times (t_{\text{B}} + t_{\text{U}}) \qquad \text{(S11)}$$

Furthermore, we modeled the amplitude of oscillation (A) by subtracting the minimum output pressure value from the maximum pressure during the oscillation. The maximum pressure calculated by taking time infinite in Eq. (S4) is given as $P(t \rightarrow \infty)$:

$$P(t \rightarrow \infty) = \frac{P_{\text{SUPP}} \times R_{\text{PULL}} + P_{\text{ATM}} \times R_{\text{BSA}}}{R_{\text{PULL}} + R_{\text{BSA}}} = P_{\text{EFF}}$$

We approximated the minimum pressure value as P_{UNFOLD} from experimental observation and derived the analytical expression for the amplitude of the oscillation as Equation S12:

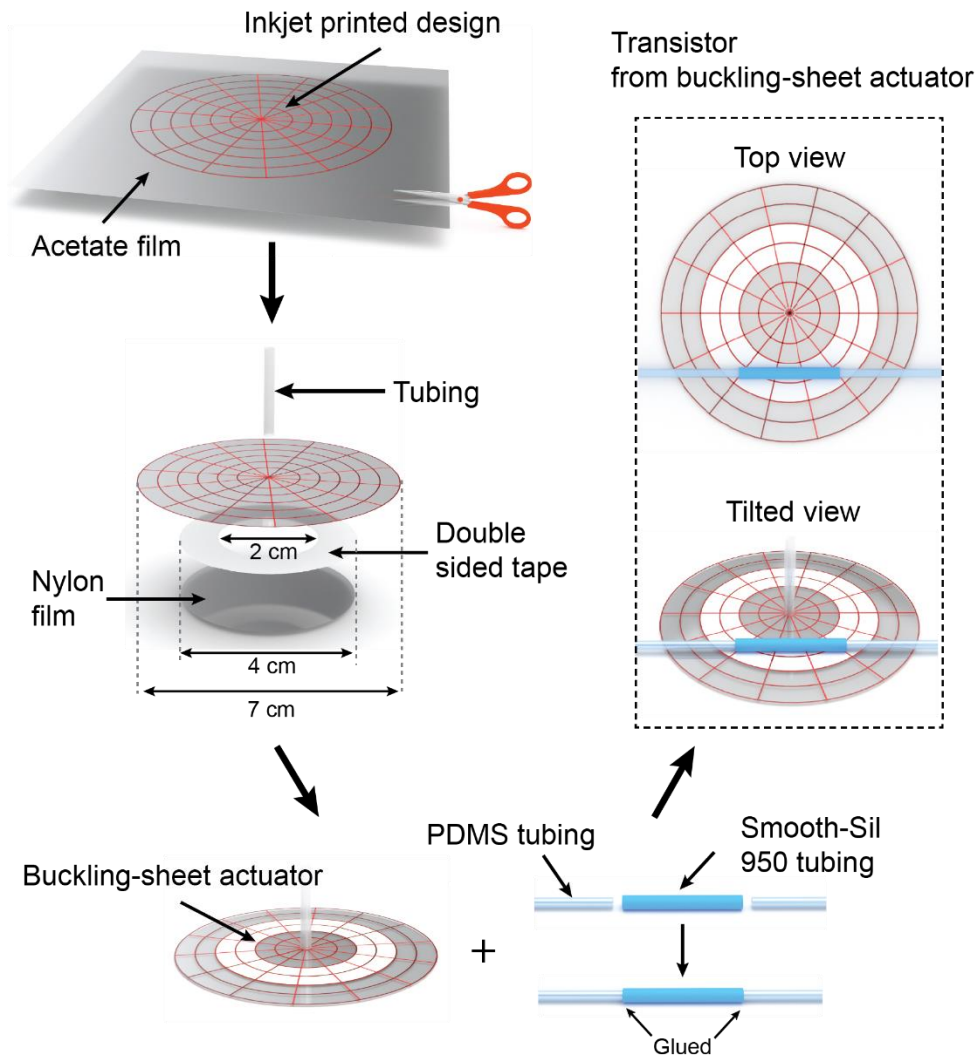$$A = P_{\text{EFF}} - P_{\text{UNFOLD}} \qquad \qquad \text{(S12)}$$

Fig. S1. Fabrication of the pneumatic switch based on buckling-sheet actuator. The circular design with the red stripes of the buckling-sheet actuator was inkjet printed on a poly(cellulose acetate) sheet, and the sheet was cut with a laser cutter or scissors. Then, a circular pneumatic bladder of Nylon film was attached at the center of the designed acetate sheet with double-sided tape. Thin rubber tubing connects the bladder to an external pneumatic source. To fabricate a pneumatic switch and inverter from the buckling sheet, a pneumatic flow-control tube was attached on the surface of buckling sheet, across the buckling position.
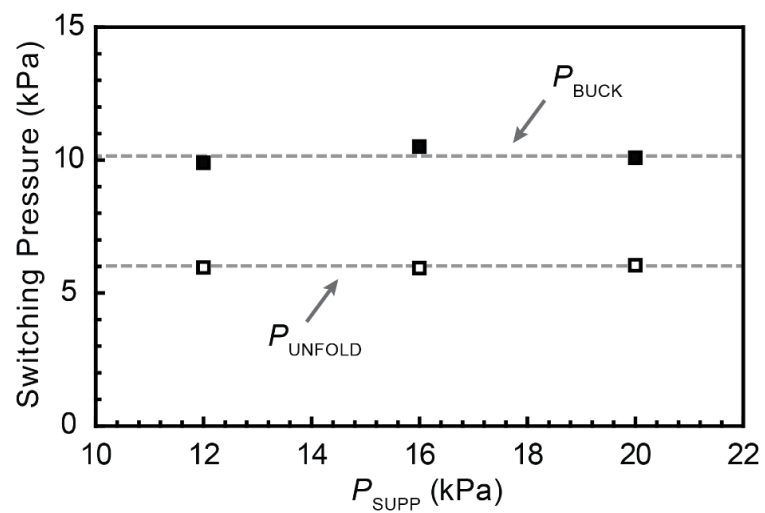
Fig. S2. P_{SUPP} does not influence the critical pressures. The critical switching pressures, P_{BUCK} and P_{UNFOLD}, were shown experimentally to be independent of the supply pressure, P_{SUPP}.
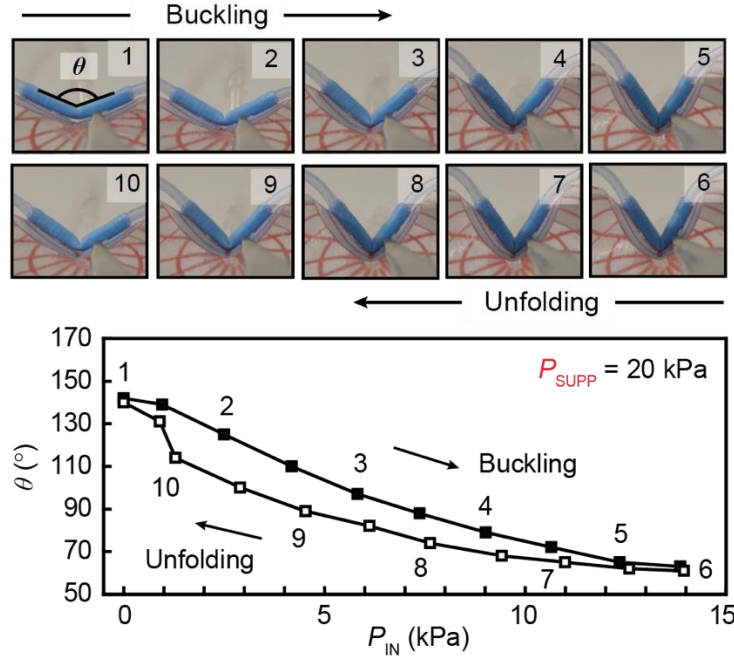
Fig. S3. Switching behavior of buckling-sheet inverter with geometric hysteresis. The bending angle (θ) of the pneumatic flow-control tube at the center of the buckling position was measured during invert switching of buckling-sheet inverter with P_{SUPP} of 20 kPa. During the buckling process, θ decreased with input pressure, P_{IN}, from $\theta = 145°$ to $\theta = 75°$ when the tube completely kinks and prevents the flow of air (stage 1 to 4). Then, θ further decreased as P_{IN} increased beyond P_{BUCK} down to a minimum value of $\theta = 60°$ (stage 6). As the buckling-sheet inverter unfolds, θ increases from the minimum value to 90° as P_{IN} decreases to P_{UNFOLD} (stage 9). The θ values during unfolding are always smaller than those during buckling with the same P_{IN} (stage 10), giving rise to the geometric hysteresis.
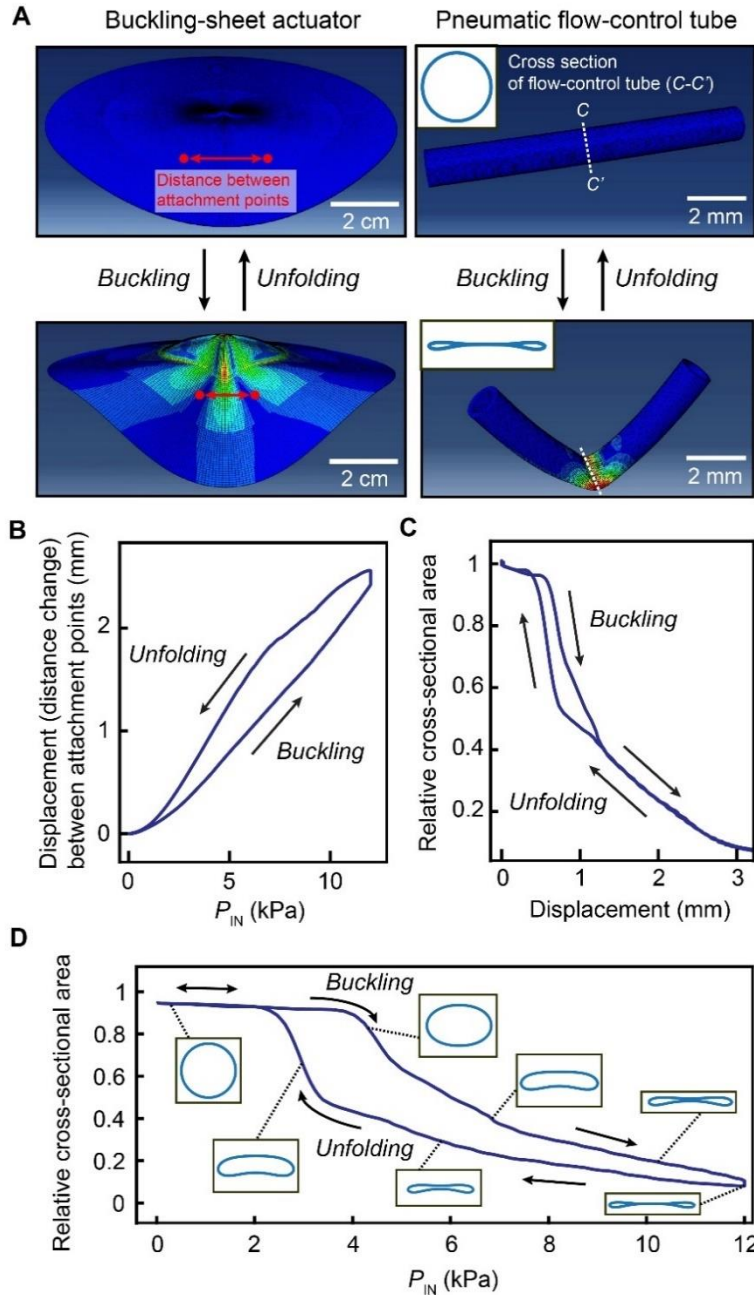
Fig. S4. Finite element method (FEM) models of the buckling-sheet inverter. Captured FEM images of the buckling-sheet actuator (left) and the attached pneumatic flow-control tube (right) **(A)**. From the FEM of the buckling-sheet actuator, the displacement (or distance change) between attachments points of the tubing, i.e. between the red points in (A), was calculated as a function of input pressure (P_{IN}) to the bladder during the buckling and unfolding of the sheet **(B)**. From the FEM model of the flow-control tube, the relative cross-sectional area at the center of the tube was estimated by inserting the displacement values from (B) into the model **(C)**. The global behavior of the buckling-sheet inverter showed that the cross-sectional deformation of the central part of the tube varied with P_{IN} with hysteresis behavior similar to that observed during experiments **(D)**.
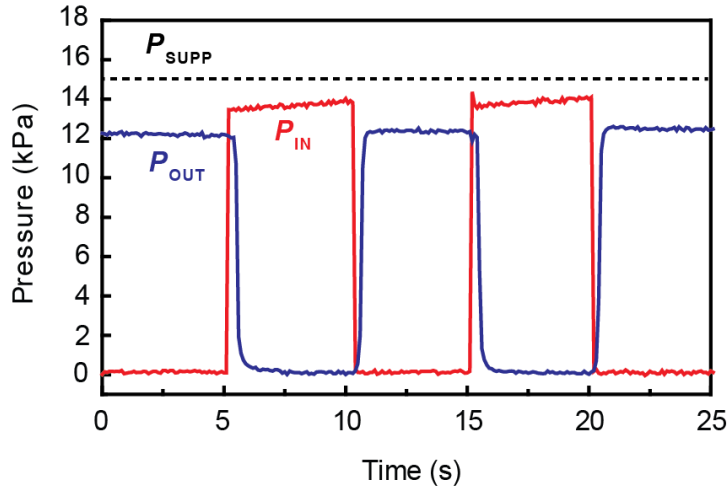
Fig. S5. Characterization of the buckling-sheet inverter by alternating P_{IN}. When the signal of P_{IN} is applied to the buckling-sheet inverter with a time interval of 5 s on and 5 s off under constant P_{SUPP}, the buckling-sheet inverter inverts the input signal, with P_{OUT} taking the opposite value of the input (a high output from a low input, and vice-versa). The P_{OUT} was lower than P_{SUPP} because of the pressure drop associated with the pulldown resistor.
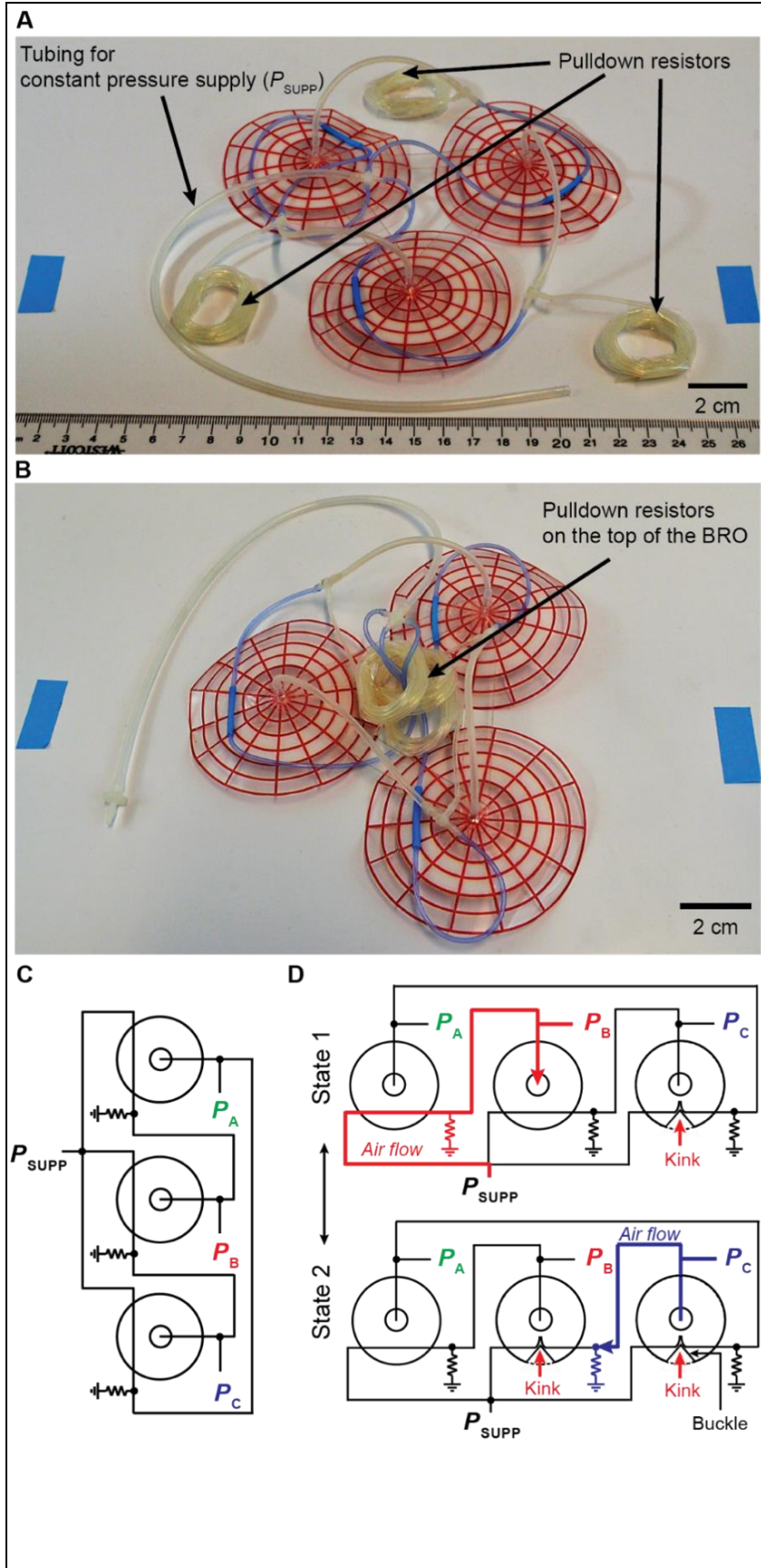
Fig. S6. Assembly of BRO and operating mechanism. The photo of a BRO-based system shows three buckling-sheet inverters connected in a loop, where P_{OUT} of one constituent inverter acts as P_{IN} of the next inverter. To create the "ring," P_{OUT} from the last inverter in the series is connected to P_{IN} of the first inverter (**A**). For locomotion, the pulldown resistors were loaded on the top of the BRO (**B**). A corresponding pneumatic circuit analog shows formation of a ring oscillator using three pneumatic inverters (disks) and pulldown resistors grounded with atmospheric pressure (**C**). When P_{SUPP} is first applied to the system, no stable state exists for the oscillation, but after a period of ~ 2 s, a pneumatic instability forms and travels around the ring as inverters sequentially buckle and unfold. The ring oscillator always contains either two adjacent unfolded inverters (with one inverter buckling, shown in state 1), or two adjacent buckled inverters (with one inverter unfolding, shown in state 2) (**D**).
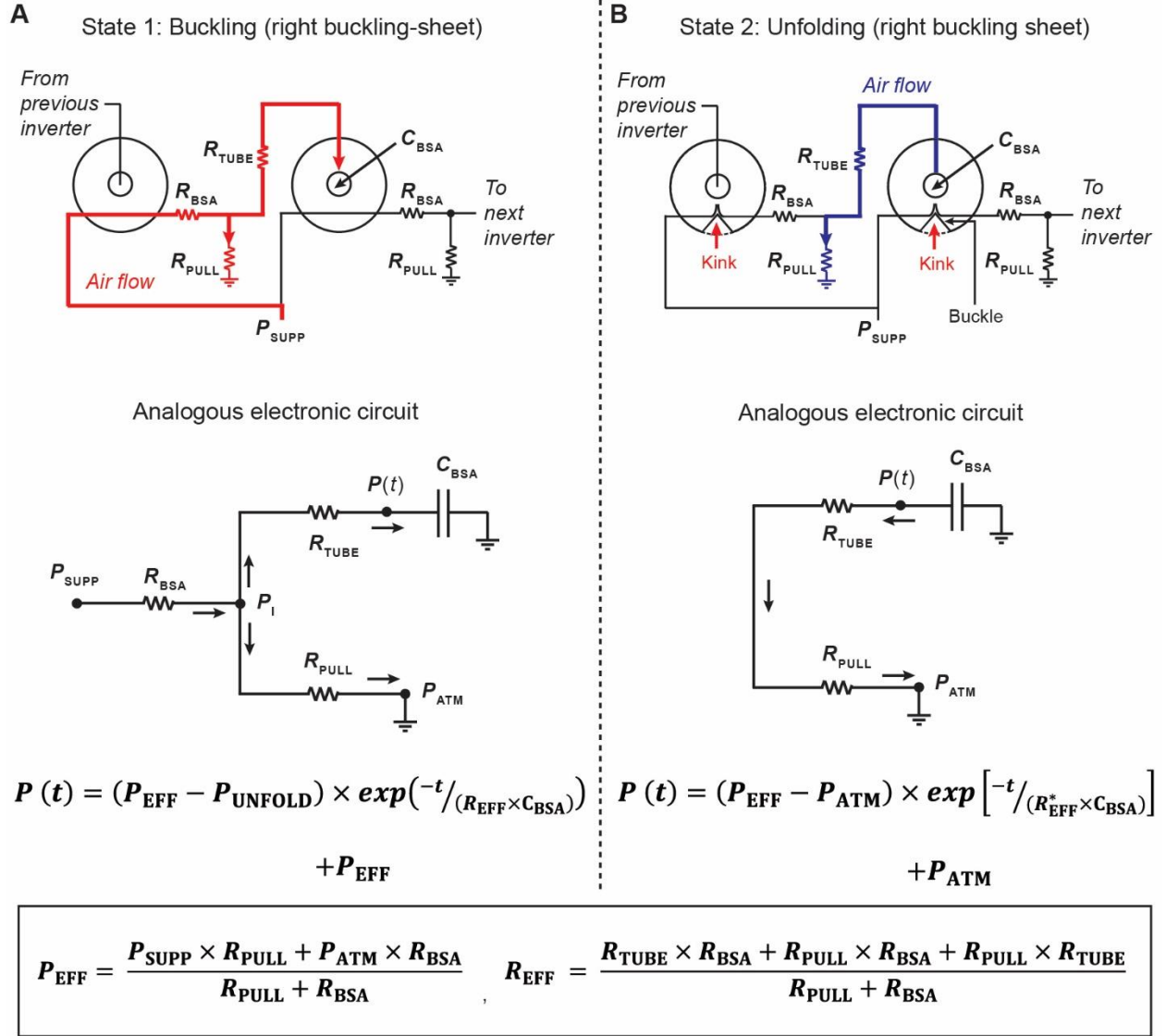
A State 1: Buckling (right buckling-sheet)

From previous inverter

R_{TUBE}

C_{BSA}

R_{BSA}

To next inverter

R_{PULL}

R_{BSA}

R_{PULL}

Air flow

P_{SUPP}

Analogous electronic circuit

$P(t)$

C_{BSA}

R_{TUBE}

P_{SUPP} R_{BSA}

P_I

R_{PULL}

P_{ATM}

$$P(t) = (P_{EFF} - P_{UNFOLD}) \times exp\left(^{-t}/_{(R_{EFF} \times C_{BSA})}\right)$$
$$+ P_{EFF}$$

B State 2: Unfolding (right buckling sheet)

From previous inverter

Air flow

R_{TUBE}

C_{BSA}

R_{BSA}

To next inverter

Kink R_{PULL}

R_{BSA}

Kink R_{PULL}

Buckle

P_{SUPP}

Analogous electronic circuit

$P(t)$

C_{BSA}

R_{TUBE}

R_{PULL}

P_{ATM}

$$P(t) = (P_{EFF} - P_{ATM}) \times exp\left[^{-t}/_{(R^*_{EFF} \times C_{BSA})}\right]$$
$$+ P_{ATM}$$

$$P_{EFF} = \frac{P_{SUPP} \times R_{PULL} + P_{ATM} \times R_{BSA}}{R_{PULL} + R_{BSA}} \qquad R_{EFF} = \frac{R_{TUBE} \times R_{BSA} + R_{PULL} \times R_{BSA} + R_{PULL} \times R_{TUBE}}{R_{PULL} + R_{BSA}}$$

Fig. S7. Analytical model for a BRO based on an electronic RC circuit analog. Pneumatic and analogous electronic RC circuits, with the analytical solutions of time varying pressure inside the buckling-sheet inverter, $P(t)$, for both states during buckling **(A)** and unfolding **(B)**. The circuit shown in **(B)** does not have a connection to the left side, towards the supply pressure, because it is adjacent to a buckling-sheet inverter in the buckled state preventing a pneumatic connection. The solutions were derived using boundary conditions for the oscillation as described in the Supplementary Text.
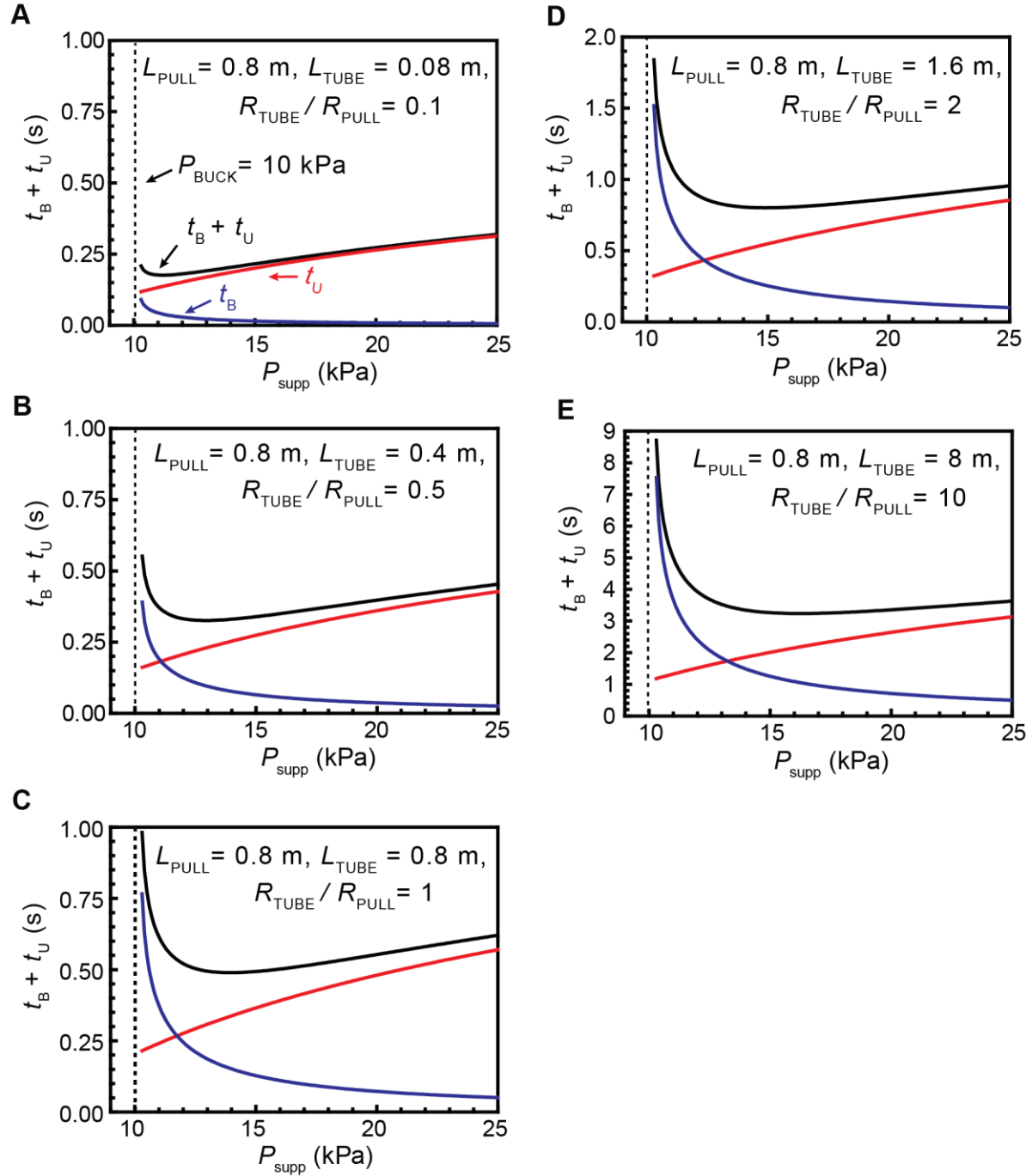
Fig. S8. Oscillation period vs. P_{SUPP} with varying pneumatic parameters. The period predicted from the model, shown here as the sum of buckling time (t_B) and unfolding time (t_U), as a function of P_{SUPP} with different pneumatic resistor ratios of R_{TUBE}/R_{PULL} of 0.1 (**A**), $R_{TUBE}/R_{PULL} = 0.5$ (**B**), $R_{TUBE}/R_{PULL} = 1$ (**C**), $R_{TUBE}/R_{PULL} = 2$ (**D**), and $R_{TUBE}/R_{PULL} = 10$ (**E**).
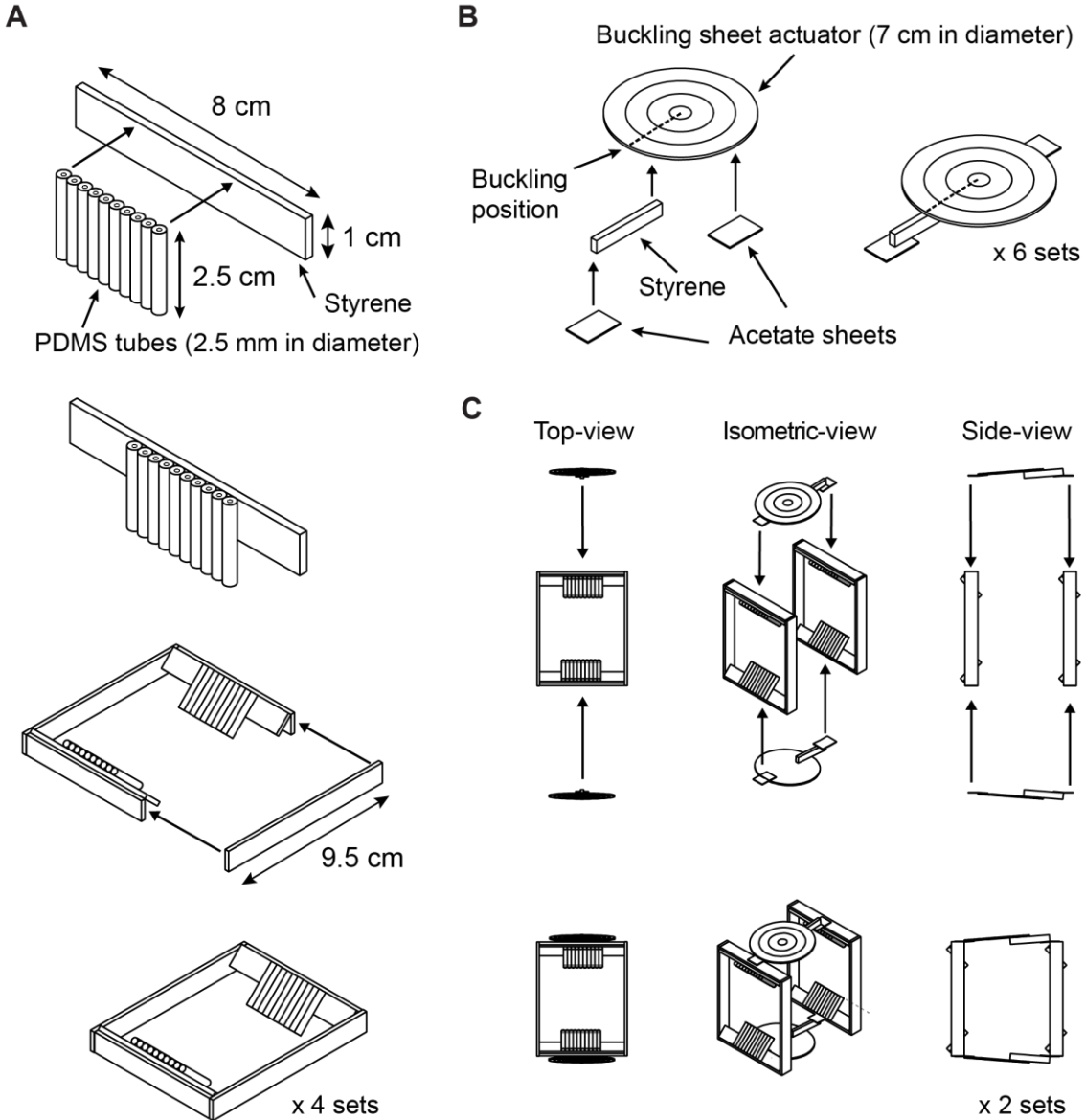
Fig. S9. Design and assembly of the beam-climber robot (steps 1-3). PDMS tubes were attached to a length of styrene with super glue to form each "foot" that contacts the beam. Then this length was glued into a rectangular frame (with hot glue) such that the PDMS tubes could contact a beam at a 45° angle, resulting in asymmetric friction behavior of each foot (**A**). Six actuators were constructed by gluing a thin piece of styrene along the "programmed" buckling point (folded by hand) in the buckling sheet actuator. Acetate sheets were then attached to the length of styrene and the other side of the buckling sheet actuator to be used as mounting points (**B**). A pair of actuators were connected to two frames, taping the acetate mounting points to the frames. This process was repeated with the remaining two frames and a second pair of actuators (**C**).
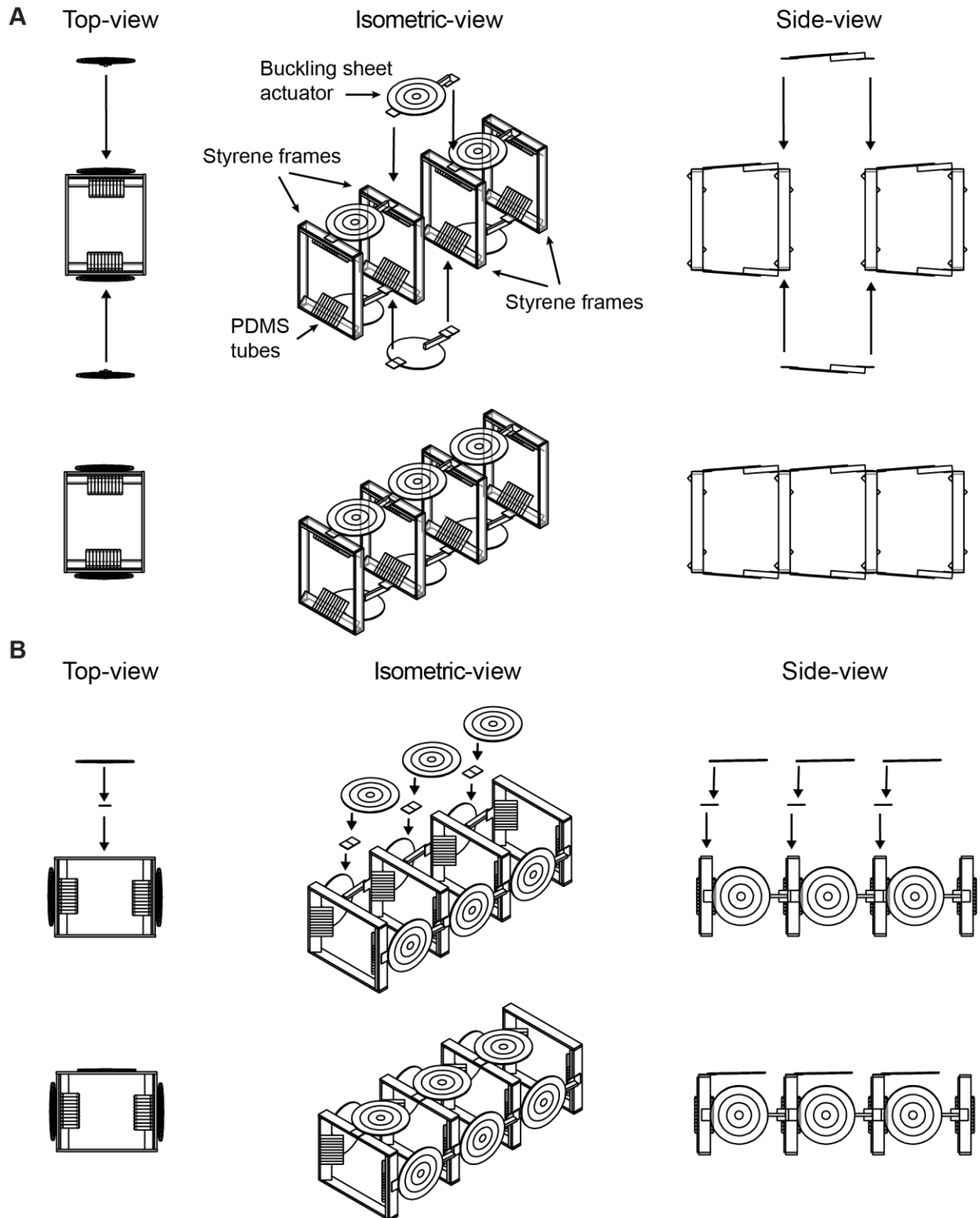
A

Top-view Isometric-view Side-view

Buckling sheet actuator →

Styrene frames

Styrene frames

PDMS tubes

B

Top-view Isometric-view Side-view

Fig. S10. Design and assembly of the beam-climber robot (steps 4-5). The two sections shown in Fig. S9C were connected using the two remaining actuators by taping the acetate mounting points to the two frames **(A)**. The BRO was then attached to the robot by taping its constituent buckling-sheet inverters to the front three frames using double-sided tape **(B)**.
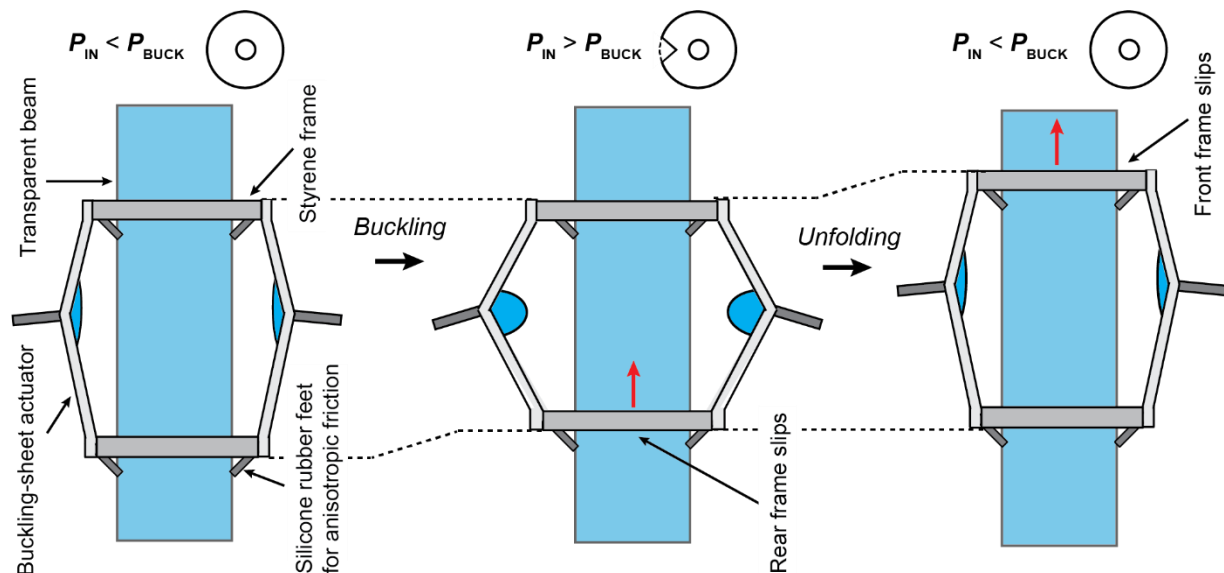
Fig. S11. Schematic illustration of beam climbing process. Each of the three unit cells of the beam-climber robot achieves climbing behavior as shown: (i) when the internal buckling-sheet actuator (BSA) pressure increases above P_{BUCK}, the BSA contracts in the vertical direction, but only the lower frame is able to move due to the asymmetric friction at the feet contacting the beam (center image); (ii) then, when the internal buckling-sheet actuator (BSA) pressure decreases below P_{BUCK}, the BSA extends in the vertical direction, but only the upper frame is able to move, again due to the asymmetric friction at the feet contacting the beam (right image). These oscillations in pressure within each of the three units of the beam-climber robot are driven by each the three outputs of the BRO, respectively.
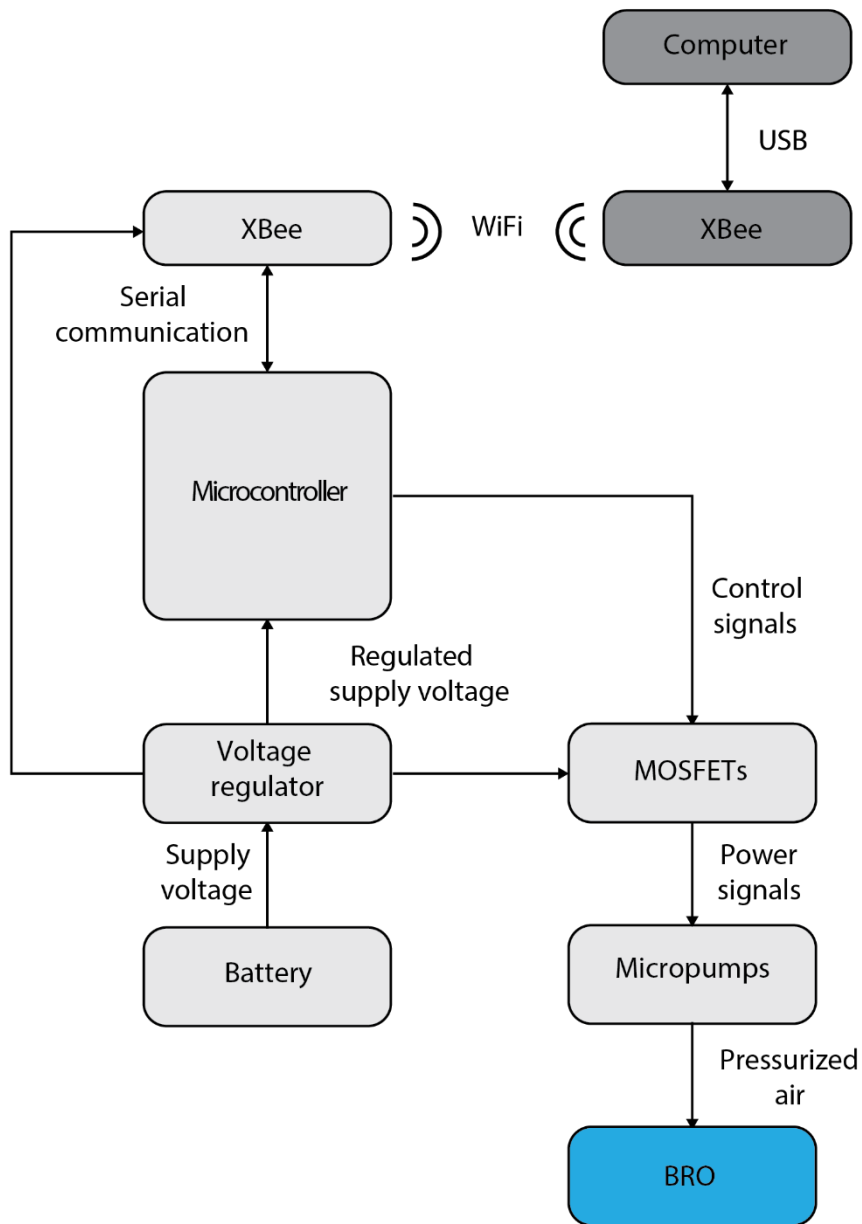
Fig. S12. Circuit design for untethered BRO. This schematic shows the individual components of our custom-made circuit used to operate BRO. A lithium-ion battery is connected to a voltage regulator, and the regulator supplies a constant voltage to the electronics. A microcontroller enables communication with a computer via X-Bee modules to switch two micropumps using a dual-channel MOSFET circuit.
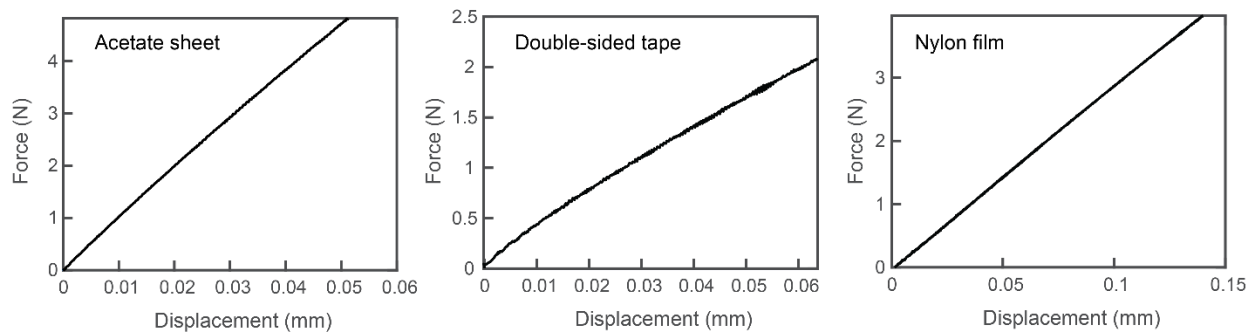
Fig. S13. Tensile tests on the materials. A linear regression was performed on the tensile data to determine Young's moduli of the different materials with values: 2.13GPa (acetate sheet), 0.32GPa (double-sided tape), 2.35GPa (Nylon film).

Table S1: Initial dimension of the tensile test specimens.

Material	Width (mm)	Length (mm)	Thickness (mm)
Acetate sheet	12.4	25.3	0.09
Double-sided tape	12.4	25.3	0.2
Nylon film	12.4	25.3	0.025

Table S2: Summary of all abbreviations in the main text.

Abbreviations	Meaning in the main text
BSA	Buckling-sheet actuator
BRO	Buckling-sheet ring oscillator
P_{IN}	Input pressure to the bladder of a buckling-sheet actuator
P_{BUCK}	Upper threshold value of input pressure (P_{IN}) for the complete buckling of a buckling-sheet actuator
P_{UNFOLD}	Lower threshold value of input pressure (P_{IN}) for the unfolding of a buckling-sheet actuator
P_{SUPP}	Constant supply pressure at the inlet of the flow-control tube
P_{OUT}	Variable output pressure at the outlet of the flow-control tube
P_{ATM}	Atmospheric pressure (pneumatic ground)
P_{EFF}	The effective pressure of the pneumatic circuit for a buckling-sheet ring oscillator
R_{EFF}	The effective resistance of the pneumatic circuit for a buckling-sheet ring oscillator
R_{PULL}	The pneumatic resistance from the pulldown resistor
R_{TUBE}	The inter-device pneumatic resistance
R_{BSA}	The pneumatic resistance from the flow control tube on a buckling-sheet actuator
C_{BSA}	The pneumatic capacitance of a buckling-sheet actuator
t_B	The buckling time for a buckling-sheet inverter
t_U	The unfolding time for a buckling-sheet inverter

Movie S1.
FEM for buckling-sheet actuator.

Movie S2.
FEM for the pneumatic flow-control tube attached on the buckling-sheet actuator.

Movie S3.
Translational motion of BRO.

Movie S4.
Rotational motion of BRO.

Movie S5.
Hybrid motions of twinned BROs.

Movie S6.
Crawling motion of BRO on sand.

Movie S7.
Swimming motion of BRO on water surface.

Movie S8.
Untethered motion of BRO on pool table.

Movie S9.
Motion of beam climber robot (0° tilting of the beam).

Movie S10.
Motion of beam climber robot (45° tilting of the beam).

Movie S11.
Motion of beam climber robot (90° tilting of the beam).

Movie S12.
Diving motion of beam climber robot with underwater cleaning.